Advanced Composites and Hybrid Materials (2024) 7:224
https://doi.org/10.1007/s42114-024-01039-6

RESEARCH

Meta-structure of amorphous-inspired 65.1Co28.2Cr5.3Mo lattices augmented by artificial intelligence

Seong Je Park[1] · Woongbeom Heogh[2] · Jeongho Yang[3] · Sukhyun Kang[4] · Wonjong Jeong[5] · Hoyoung Lee[6] · Tae-Sik Jang[7] · Hyun-Do Jung[8] · Mohammad Jahazi[9] · Seung Chul Han[10] · Hyoung Seop Kim[11,12,13] · Myoung-Gyu Lee[6] · Susmita Bose[14] · Amit Bandyopadhyay[14] · Martin Byung-Guk Jun[15] · Young Won Kim[15] · Xingyu Fu[15] · Rigoberto C. Advincula[16,17,18] · Clodualdo Aranas Jr.[19] · Sang Hoon Kim[20]

Received: 2 January 2024 / Revised: 9 March 2024 / Accepted: 21 October 2024 / Published online: 6 November 2024

Abstract
A hatching-distance-controlled lattice of 65.1Co28.2Cr5.3Mo is additively manufactured via laser powder bed fusion with a couple of periodic and aperiodic arrangements of nodes and struts. Thus, the proposed lattice has an amorphous-inspired structure in the short- and long-range orders. From the structural perspective, an artificial intelligence algorithm is used to effectively align lattices with various hatching distances. Then, the metastable lattice combination exhibits an unexpectedly high specific compression strength that is only slightly below that of a solid structure. From the microstructural perspective, the nodes in the newly designed lattice, where the thermal energy from laser irradiation is mainly concentrated, exhibit an equiaxial microstructure. By contrast, the struts exhibit a columnar microstructure, thereby allowing the thermal energy to pass through the narrow ligaments. The heterogeneous phase differences between the nodal and strut areas explain the strength-deteriorating mechanism, owing to the undesirable multi-phase development in the as-built state. However, solid-solution heat treatment to form a homogeneous phase bestows even higher specific compression strength. Furthermore, electrochemical leaching leads to the formation of nanovesicles on the surface of the microporous lattice system, thereby leading to a large surface area. A more advanced valve cage for use in a power plant is designed by using artificial intelligence both to (i) effectively preserve its mechanical stiffness and (ii) actively dissipate the generated stress through the large surface area provided by the nanovesicles.

Keywords Hatching-distance-controlled lattice · Amorphous-inspired structure · Metastable lattice combination · Heterogeneous phase differences · Artificial intelligence

1 Introduction

A hatching-distance-controlled microporous lattice consisting of broadly and densely distributed nodes and highly raveled and entangled struts is additively manufactured via laser powder bed fusion (LPBF). The uniform distribution of pores and random arrangement of ligaments are repeated through precise laser control to several hundreds of micrometers. The microporous lattice has unexpectedly strong resistance to external pressure and force due to the unique strengthening mechanism [1]. From a morphological perspective, this can be explained by the amorphous-inspired, glass-like form, in which the nodes have a certain level of short-range translational periodicity but are highly conjugated by the struts, which exhibit long-range aperiodicity [2]. Meanwhile, from a structural perspective, an external load can be resisted to an extent that depends more on the nodal connectivity than on the strut constitution, despite the low relative density (lightweight characteristic) of the material [3]. In addition, the microporous lattice is provided with a large surface area due to the formation of nanovesicles thereon after electrochemical leaching.

Upon rapid solidification with a high cooling rate in the range of 10^4 to 10^7 K s^{-1}, the additively manufactured 65.1Co28.2Cr5.3Mo lattice structure (with the nominal chemical composition of Co-based Inconel) exhibits a combination of face-centered-cubic (fcc) and hexagonal close-packed (hcp) phases [4, 5]. The small fraction of hcp phase

Seong Je Park and Woongbeom Heogh contributed equally to this work.

Extended author information available on the last page of the article

is stabilized well beyond the minimum required tolerance due to repeated thermal cycling during continuous laser irradiation annealing of the entire structure [6]. Furthermore, there are clear differences between the phases in the nodal and strut areas in the cellular structure [7, 8]. In the nodal area, the thermal energy generated by laser irradiation cannot flow because it is insulated by the adjacent powder with low thermal conductivity [7, 8]. Moreover, the abnormally large equiaxial dendrites that commonly appear in the as-cast microstructure are present, along with the secondary phases (ε-hcp, segregates, and precipitates) [4, 5, 9]. Comparatively, the strut area is mainly composed of the primary γ-fcc phase because the thermal energy can rapidly and easily proceed along the thin ligament pathway [4, 5]. Thus, the negative interactions between the two neighboring (heterogeneous) phases deteriorate the microstructural uniformity, particularly at the interfacial boundaries, thereby leading to concentrated residual and thermal stresses [10, 11]. This, in turn, significantly decreases the deformation resistance, particularly concerning the compression strain [10–12]. However, tailoring the heterogeneous mixture of primary and secondary phases to a more homogeneous microstructure through heat treatment (HT) ultimately provides the novel lattice with superior mechanical strength [10, 11].

Based on the lattice integration and microstructural unification, an artificial intelligence (AI) algorithm is required in order to configure the metastable alignment of the amorphous-inspired lattices. In particular, we determine how the as-determined metastructure of the lattice combination leads to an abnormally high elastic modulus compared to the relative density (i.e., an unexpectedly high specific compression strength). Thereafter, we apply the hierarchical lattice system to the outer plate of a topologically optimized valve cage used in a power plant after identifying the stress-bearing regions and removing the unnecessary stress-free regions. Subsequently, AI is simultaneously applied to design a compatible lattice alignment that offers high mechanical stiffness along with a large surface area. In this respect, the AI-based design satisfies the conflicting requirements of auxiliary strength along with the ability to extract the residual and thermal stresses that accumulate due to the heat generated inside the valve cage when recycling hot and cold fluids.

2 Experimental

2.1 Additive manufacturing of the solid and lattice structures

Before the process, a vacuum of around 1×10^{-3} torr was created, and then a protective atmosphere (< 100 ppm of oxygen) was then backfilled to approximately 1 atm. All of the solid and lattice structures with different hatching distances (80 (solid), 150, 200, 250, 300, 350, 400, 450, 500, 550, 600, 650, 700, 750, or 800 μm (lattices)) were additively manufactured by applying a laser intensity of 170 W, layer thickness of 40 μm, spot size of 80 μm, and laser speed of 1.4 mm s^{-1}. The build rates were around 5–20 cm^3 h^{-1}, according to the structural composition. A specific layer orientation (245° rotation per layer) was used for laser irradiation to develop the 65.1Co28.2Cr5.3Mo structures on an identical 65.1Co28.2Cr5.3Mo substrate with a diameter of 250 mm and thickness of 10 mm. The additively manufactured 65.1Co28.2Cr5.3Mo structures were electrochemically leached (5.0 V and 0.2 A) in a hydrogen chloride solution (containing 50 wt.% each of H_2O and HCl) to (i) remove the remaining powder loosely solidified on the inner and outer grids and (ii) form the nanovesicles on their surfaces. Subsequently, the powder-free structures were solid-solution-treated at 1200 °C for 2 h, followed by rapid cooling to 25 °C within 10 min via gas quenching, aging at 500 °C for 30 min, and slow cooling to 25 °C in a furnace.

2.2 Physical evaluation and chemical characterization

The chemical composition of the 65.1Co28.2Cr5.3Mo powder was measured using an inductively coupled plasma–optical emission spectrometer (ICP–OES; Optima 8300, Perkin Elmer, USA). The concentrations of oxygen and carbon contained in the 65.1Co28.2Cr5.3Mo powder were determined using an oxygen/nitrogen analyzer (ON–900, Eltra GmbH, Germany) and a carbon/sulfur analyzer (CS–800, Eltra GmbH, Germany), respectively. The powder's particle size distribution was determined using a particle size analyzer (PSA; LS13 320, Beckman Coulter Inc., USA) equipped with a laser-driven scattering measurement detector. High-precision X-ray microcomputed tomography (μ-CT; v|tome|x M300, Baker Hughes Company, USA) was employed to investigate the presence and absence of the remaining powder embedded in the lattice after electrochemical leaching. The μ-CT system was operated at 300 kV with a micro-focus tube and 180 kV with a nano-focus tube to scan the inside of the lattice. The morphology of the precursor powder and microstructures of the additively manufactured structures were studied using scanning electron microscopy (SEM; JSM–5800, JEOL, Japan). Electron backscattering diffraction (EBSD) analysis was carried out using SEM (SU70, Hitachi, Japan) equipped with an accessory (NordlysNano, Oxford, UK) to investigate the grain orientations in the solid and lattices before and after HT. The diffraction patterns and elemental compositions of the different regions of the as-built lattice structure with a hatching distance of 800 μm were determined by selected area electron diffraction (SAED) and energy-dispersive X-ray spectroscopy (EDS) with transmission electron microscopy (TEM; JEM–ARM200F, JEOL, Japan). The crystalline phase changes in the powder and structures were determined via

X-ray diffraction (XRD; D/Max–2500VL/PC, Rigaku International Corp., Japan) analysis at 40 kV and 250 mA over a 2θ range of 20–90°. Roughness testing (SJ–410, Mitutoyo, Japan) to determine the degree of evenness and regularity on the top planes of the solid and lattice structures was conducted with a passing speed of 0.1 mm s^{-1} and measured distance of 5.0 mm while applying a diamond tip. The heat transfer coefficients of the solid and lattice structures were measured as a function of temperature by using a disc-type thermometer in an insulated container. The specific surface area was determined via N_2 adsorption/desorption isotherms based on the Brunauer–Emmett–Teller (BET) method by using the analysis port of a physisorption and chemisorption analyzer (Autosorb–iQ, Quantachrome Instruments, USA).

2.3 Compression testing

The compression testing for all the solid and lattices was simply regulated according to the American Society for Testing and Materials (ASTM) E9 – 09. The single-modal (hatching distances of 80, 200, 400, 600, or 800 μm) and multi-modal (2-, 4-, or 8-lattice combinations with thin boards of 0, 1, or 2 mm) solid and lattice structures fabricated using LPBF were prepared for compression testing by using a universal testing machine (Insight–100, MTS Systems, USA) at room temperature under a crosshead speed of 2.0 mm min^{-1}. The solid and lattice structures having different hatching distances can be classified by their most prominent deformation mechanism during compression testing, that is, either bending or stretching. In the compressive (engineering) stress–strain curves, the solid and lattices with a hatching distance of 200 μm or less exhibited bending-dominant structures. By contrast, those with a hatching distance of 400 μm or more exhibited stretching-dominant structures from a morphological perspective, increasing their structural load-bearing capacities. However, the geometrical perspective was different. Thus, the conventional cellular structures adopted bending- or stretching-dominant structures according to their unit cell geometries; for example, the diagonal, diamond, and gyroid structures are bending-dominant, whereas the octahedral, octet, and kagome structures are stretching-dominant. When subjected to compressive stress, the structure exhibits the linear elastic modulus behavior with the gradient representing its coefficient value until its elastic limit, after which the yield point is exceeded and the structure bends or stretches and eventually fractures. From a mechanical perspective, the elastic modulus of the bending-dominant cellular structure in particular is given by Eq. (1):

$$\widetilde{E} / E_s \approx (\widetilde{\rho} / \rho_s)^2, \tag{1}$$

where $\widetilde{E}$ is the elastic modulus of the cellular structure, E_s is the elastic modulus of the solid, $\widetilde{\rho}$ is the density of the cellular structure, and ρ_s is the density of the solid. Comparatively, when subjected to compressive stress, the elastic modulus of the stretching-dominant cellular structure is linearly proportional to its relative density and can be described by Eq. (2):

$$\widetilde{E} / E_s \approx (\widetilde{\rho} / \rho_s)^1, \tag{2}$$

where the same indexes, given in Eq. (1), are used as the parameters of the cellular structure. In the compression testing, the relationship between the elastic modulus and the relative density distinguishes the bending- or stretching-dominant cellular structure. The elastic modulus and initial yield strength of the stretching-dominant cellular structure are typically considerably higher than those of the bending-dominant cellular structure with the same relative density, which makes the former structure attractive for use in lightweight structural components. Meanwhile, Maxwell's stability criterion also gives the condition under which the structure primarily deforms by bending or stretching. Specifically, the question of whether the lattice structure is bendable or stretchable is determined by the standard stability equation for the 3D structure, given here as Eq. (3):

$$M = b - 3j + 6 \geq 0, \tag{3}$$

where j and b denote the numbers of nodes and struts, respectively, in the unit cell. Nevertheless, the boundaries of the nodes and struts in the hatching-distance-controlled lattice structures are ambiguous, and their counting is even more challenging. In addition, the node connectivity of the cellular structure plays an important role in defining its deformation mechanism. For example, the node connectivity Z of an octet truss unit cell with an fcc cellular structure is $Z = 12$. This type of connectivity offers stretching-dominant deformation. Finally, the area under the compressive stress–strain curve from the initial stage up to the densification strain is evaluated as the energy absorbed by the structure. The specific energy absorption (ψ) is defined as the work (W) performed per unit density when the lattice is compressed in a uniaxial manner up to the ultimate strain or fracture strain, as given by Eq. (4):

$$\psi = W/\rho = \int_0^{end} \sigma d\varepsilon, \tag{4}$$

where ρ denotes the mass density, σ is the axial stress, and ε is the work-conjugated strain. Furthermore, the compression behaviors of the single-modal structures with hatching distances of 80 (solid), 400, or 800 μm were analyzed using a commercial finite element analysis (FEA) software package (Abaqus, Dassault Systèmes Simulia Corp., France) and compared to those reported experimentally. The linear static analysis was performed only in the elastic region for finite element modeling (FEM) to confirm the compression

behaviors of the solid and lattices. The finite element type was performed based on a four-node three-dimensional (3D) tetrahedron element. The number of meshes was 112,965 for the solid. The lattices with hatching distances of 400 and 800 μm were composed of 1,865,743 and 776,335 meshes, respectively. No friction occurred in the regions where all the nodes and struts in the hatching-distance-controlled lattices were connected. Consequently, each lattice was combined and modeled to become a single model. To evaluate the feasibility of applying deep learning (Python, Python Software Foundation, USA), a convolutional neural network (CNN) was utilized as a more advanced structure design strategy to develop a complex 12-lattice combination using the solid and lattices with hatching distances of 80, 200, 300, 400, 500, 600, 700, and 800 μm to ensure a yield strength of 300.0 MPa and thin board of 1 mm as an example. After using the CNN to determine the 12-lattice combination with an intercalating layer of 1 mm comprising 700/300/400/500/300/600/300 (7 lattices in the upper block) and 300/800/300/600/300 (5 lattices in the lower block), FEM was employed to simulate the target yield strength of the lattice combination based on previous single- and multi-modal compression testing. It arranged the intercalating layer between the upper and lower blocks. The high specific compression strength is specifically derived from a network of nearly balanced lattices that are partitioned by the 1-mm-thick intercalating layer. Thus, each lattice can be considered as a unit cell (building-block) of the cellular structure. Moreover, each lattice is aligned so as to effectively resist the external load under compression, even though the unit cell itself exhibits the amorphous-inspired, glass-like structure. Due to the equivalent stress gradient distribution of the lattice combination according to the coordinated partitioning, it was postulated that the 12-lattice structure with 7 lattices in the upper block and 5 lattices in the lower block would produce a yield strength of close to 300.0 MPa. This was computationally verified by the FEM analysis. Subsequently, the actual yield strength of the lattice combination in the experiment was measured and compared to the calculated simulation result. This is an example of the use of deep learning to design a meta-structure based on the desired yield strength, along with the subsidiary application of FEA to simulate the compression testing of the meta-structure, and the experimental confirmation of the statistical and simulation results of the additively manufactured meta-structure.

2.4 Topological optimization and strategic alignments of the solid and lattice structures

A 3D scanner (ZS–3040, Laser Design Inc., USA) replicated the original valve cage used in the power plant. The original part was fabricated via casting, forging, and machining. Anti-glare powder was sprayed onto the structure's surface to suppress laser reflection, facilitating more accurate 3D scanning. The data were obtained as an ASC file comprising point clouds. The file was transformed into an STL file by combining meshes, followed by a final change into an STP file comprising faces and solids. Subsequently, FEM was employed to simulate an equivalent stress distribution on the original part, and topological optimization was utilized to develop a novel part in which the stress-bearing regions in the original part were maintained, and the unnecessary (stress-free) regions were eradicated. In other words, topological optimization minimizes the structural compliance (maximizes the deformation resistance), thus resulting in a reduced volume. The technique used in the present study is based on a solid isotropic material with penalization (SIMP), which is dependent on mesh fidelity; SIMP uses a penalized stiffness model to correlate between the volume and strength as follows:

$$E(x) = \rho(x)^{p}E^{0}, \rho > 1 \text{ and } \int_{\Omega} \rho(x)d\Omega \le V;\ 0\ \rho(x) \le 1, x \in \Omega, \tag{5}$$

where E is the elastic modulus of the element, ρ is the density of the element, p is the penalization factor, E^0 is the original elastic modulus, Ω is the designed space domain that is eligible for optimization, and *x* is the individual element. The total volume of domain optimization must be equal to or less than the volume constraint V. The equation determines the optimal space layout by iteratively changing the density of each element in the FEM. If the element is not highly stressed, the relative density decreases because the element is not necessary for structural strength, whereas if the element is highly stressed, its relative density increases to the initial volume (full relative density). As a result, the relative density of the structure is reduced by lowering the mass per original volume while maintaining the structural feature in the design perspective. Meanwhile, the thermal energy gradient distribution of the topologically optimized part was simulated using commercially available fluid dynamics analysis software (FLOW–3D, Flow Science Inc., USA). The CNN determined the effective alignments of 15 types of lattices (including a solid form) with hatching distances of 80, 150, 200, 250, 300, 350, 400, 450, 500, 550, 600, 650, 700, 750, and 800 μm to constitute the hierarchical lattice system on the outer plate of the topologically optimized valve cage. Each lattice was assigned a number, from unit cell 1 (U1) to 15 (U15), and these were then arranged into 3D configurations with 18,451 elements to make the sections similar in shape to the original part. Considering that the increased thickness of the buffer board helped improve the sustainability of the hierarchical lattice system, the thickness of the intercalating layer was controlled at each boundary between the lattices. All of the possible configurations of

3, 5, and 7 different compartments (referred to as components in programming) that produced equivalent stress and thermal energy gradient distributions were generated, along with the following three types of lattice combinations: (i) 5 lattices with hatching distances of 80 (solid), 200, 400, 600, and 800 μm; (ii) 8 lattices with hatching distances of 80 (solid), 200, 300, 400, 500, 600, 700, and 800 μm; and (iii) 15 lattices with hatching distances of 80 (solid), 150, 200, 250, 300, 350, 400, 450, 500, 550, 600, 650, 700, 750, and 800 μm, while taking a high mechanical stiffness and large surface area (50% of each maximum) into consideration. Some of these were then used as the dataset for deep learning. For example, to achieve cohesion on the outer plate with 7 components and 15 lattices with various hatching distances, the number of configurations was 15^7 (170,859,375). The dataset was determined as 17,086 (one-ten thousandth of all possible configurations). Once the CNN model learned the most effective alignment by using the lattice combinations in the dataset, it was able to accurately partition the lattices to maximize the mechanical stiffness and surface area. Based on this information, the valve cage was additively manufactured using LPBF. The human-intelligence and FEM-based meta-structures (Table 1), which were fabricated using various additive manufacturing (AM) techniques and methods, were compared to our AI-augmented meta-structure in terms of relative density and mechanical strength (thus, specific compression strength). These structures were selected based on the specific requirements of various target applications and transportation systems.

3 Results and discussion

3.1 Controlling lattice porosity by varying the hatching distance during laser irradiation and subsequently removing the residual powder by using electrochemical leaching

The photograph in Fig. 1a depicts the as-fabricated microporous lattice with a hatching distance of 800 μm, showing nanovesicles on its surface, and without any powder remaining after electrochemical leaching. The overlapping conjugation of struts provided the microporous lattice with broadly and densely distributed nodes, thereby forming relatively well-ordered periodic arrays. Thus, a deliberate application of this cellular structure resulted in a large surface area. Figure 1b presents representative μ-CT images of the lattice, whose dimensional accuracy was evaluated by considering both horizontal and vertical slices. Consistently with the intended geometrical design, the shapes of the cross-sectional struts observed in the μ-CT slices contain highly entangled aperiodic ligaments, although a few of them have already been slightly disrupted by the residual and thermal stresses that occurred after laser irradiation. Figure 1c presents a lattice, free of any remaining powder, owing to post-processing via electrochemical leaching. The powder (Fig. 1d) can loosely solidify on the inner and outer grids of the main lattice, causing energy instability [13, 14]. When such powder is present, it can deflect the cracks and/or cause the deficiencies to slide out, thereby deviating from the conventional fracture mechanism (i.e., the initiation of elastic deformation, which propagates at the expense of plastic deformation, ultimately leading to a plateau in the plastic deformation, and complete fracture) [13, 14]. Thus, removing the residual powder (Fig. 1e) increased the unprecedented specific mechanical strength of the newly created lattice (by lowering the relative density but increasing the mechanical strength and deformation resistance) [9, 15]. Figure 1r presents the measured distribution for the cross-sectional surface area, as determined from the combination of nodes with periodic translation and randomly distributed struts. The graph depicts a broad Gaussian distribution and suggests an average specific surface area of 0.012 $m^2\ g^{-1}$, which is significantly lower than the actual specific surface area of 0.226 $m^2\ g^{-1}$ determined from the BET analysis, as shown in Fig. 1s. This is because the μ-CT analysis only determined the specific surface area of the pores on the lattice, while the BET analysis included both the lattice pores and the nanovesicles on the nodes and struts [16, 17]. In detail, the laser spot size of 80 μm provided the thin nodes and struts in the lattice structure. Thus, the ligaments had an average diameter of 80 μm. In addition, the nanovesicles (with an average cellular size of 420 nm) were formed by electrochemical leaching, and were homogeneously distributed on the nanostructured surfaces, which exhibited a high specific surface area of 0.226 $m^2\ g^{-1}$. The surface roughness (R_a) of the cross-sectional variation along the axis crossing the *x*–*y* plane of the lattice was evaluated for the lattice with a hatching distance of 800 μm. As a result, the repeated alignment of the nodes and struts and vacant pores in the cellular structure yielded an average R_a value of 89.8 μm, which indicates significantly greater protuberances than on the solid ($R_a = 4.1$ μm) (Fig. 1t). In the surface roughness analysis, although there were poorly repeated peaks in a slightly routine pattern over a distance of 800 μm, indicating the presence of nodes, some peaks were missing owing to the disconnected struts. Overall, there was some variability in the presence of nodes with a certain amount of translational periodicity, which differed from the struts in an aperiodic arrangement. Figure 1u depicts the variation in the heat transfer coefficient in terms of the porosity of each lattice structure [18–21]. While the heat transfer coefficient of the solid increased linearly with increasing temperature from 400 to 700 K, owing to a pronounced

Table 1 A reference comparison of the physical and chemical properties of our AI-augmented meta-structure with those of the additively manufactured structures fabricated by LPBF, directed energy deposition, wire arc AM, etc., evaluated and classified in terms of lightweight relative density design

AM process	Alloy system	Density (g cm^{-1})	Specific applications	Manufacturing advantages	Mechanical properties	Advantageous physical properties	Key points	Ref. (No.)
LPBF	65.1Co28.2Cr5.3Mo	Low relative density (i.e., lightweight) based on the hatching distance	A valve cage for use in a power facility	The AI-augmented, cellular meta-structure manufactured by LPBF can be highly controlled in a regular order, through the precise control of the AM process and the particularly balanced collapse design of the specific lattice combination	The yield strength can be controlled by the combination of lattices with different hatching distances	High convective heat transfer using a large surface area of nanovesicles	AI configures the metastable alignment of amorphous-inspired lattices	Our study
Self-propagating photopolymer waveguide technique	Ni–P	0.9 mg cm^{-3}	Thermal insulation materials, battery electrodes, catalyst supports, and acoustic, vibration, or shock energy damping	The electroless Ni plating of ultralight materials based on periodic hollow-tube microlattices creates an even layer of metal regardless of the surface geometry	For the first compression cycle, the work done in compression was 4.6 mJ cm^{-3} and the energy dissipation was 3.5 mJ cm^{-3}, yielding an energy loss coefficient of 0.77	The metallic microlattices were designed to exhibit densities of less than 0.9 mg cm^{-3}, recovery even after compression strains of greater than 50%, and similar energy absorption to that of an elastomer	Large energy absorption upon cyclic loading	[65]
Primary fabrication of the Shellular microlattice template via a mask-based lithographical approach, followed by Ni plating, mechanical polishing, and chemical etching to provide an engraved pattern (a negative template) on the surface of the structure	Ni–P	Relative density (0.1%)	Suitable for use in thermal insulation	The mask-based lithographical approach to the fabrication of the Shellular microlattice makes it possible to avoid any structural incompleteness	The structure was meta-stable under the linear relationship between the relative elastic modulus and relative density	The Shellular microlattice was designed to have a smooth continuous surface according to the minimal surface theory in order to resist the external load due to coplanar stress	A new type of low density Shellular structure is developed	[66]

Table 1 (continued)

AM process	Alloy system	Density (g cm^{-1})	Specific applications	Manufacturing advantages	Mechanical properties	Advantageous physical properties	Key points	Ref. (No.)
Projection micro-stereolithography followed by atomic layer deposition	Amorphous Al_2O_3	Densities ranging from below 1 g cm^{-3} up to 10.2 g cm^{-3}	The 3D micro- and nanoarchitectures exhibit many beneficial mechanical, energy conversion, and optical properties	The thickness of the Al_2O_3 coating can be controlled at between 40 and 210 nm by atomic layer deposition prior to the removal of the additively manufactured polymer template via thermal decomposition	The desired linear relationship between $\widetilde{E}/E_s$ and $(\widetilde{\rho}/\rho_s)^n$, approaching the theoretical limit, was determined by the stretch-dominated microlattice	A stretch-dominated mechanical metamaterial	Improved mechanical properties can arise from a material that contains micro- and nanoscale building blocks arranged in an ordered hierarchy	[46]
Mold fabrication via a multi-jet printing method, followed by casting	Having the target mechanical properties regardless of the materials or scales	Density not stated in the study, but the structure appears to have a high-volume density	Can support the design of innovative soft robots, wearable devices, footwear, and energy-absorbing systems	AM of a highly accurate structure	Under uniaxial compression, the quadrilateral units remain rigid, and the deformation localizes at the hinges	Nonlinear mechanical response characteristics via a metamaterial platform with hinged quadrilaterals	The neural network can learn the relationship between the unit cell design and the deformed configuration and can be used in combination with an evolutionary strategy to design efficient inverse architectures	[67]
LPBF	Stainless steel 316L can be used as a base material	The relative density of the designed structure depends on the composition of the lattice	No specific applications were mentioned or demonstrated	AM improves the geometric accuracy and quality of the lattices	The strength and hardness can be controlled by the alignment of different lattices	Materials exhibiting damage-tolerant architectures with the desired strength and toughness, along with enhanced functionality and performance in response to external loads, via the combination of physical metallurgy and architected metamaterials	The lightweight and damage-tolerant architecture is inspired by the typical microstructures of crystals	[9]

Table 1 (continued)

AM process	Alloy system	Density (g cm^{-1})	Specific applications	Manufacturing advantages	Mechanical properties	Advantageous physical properties	Key points	Ref. (No.)
Two-photon polymerization-based direct laser writing	Fused SiO_2	Lightweight structures	Suitable for the design of superior engineering systems, from reusable impact protection systems to adaptive load-bearing structures	AM of a highly accurate structure by using photolithography	High mechanical stiffness and yield strength can be maintained even under cyclic compression loading	Superior deformability and energy absorption, with consistency between experimental and theoretical data	The as-fabricated structure exhibits unprecedented failure resistance, with an up to 25-fold enhancement in deformability, along with an orders of magnitude increase in the energy absorption capability compared to the same-strength state-of-the-art lattice architectures	[68]
AM of a Cu–polyimide sheet, followed by impregnation of the polyimide structures with poly(methyl methacrylate) via a wet etching technique	Cu–polyimide sheet and poly(methyl methacrylate) infiltration	Lightweight structures when using a low density of poly(methyl methacrylate)	For use in applications such as high-precision space optical systems, adaptive connecting components in satellites, battery electrodes with unique thermal expansion properties, dental fillings, thermally controlled shape-changing structures, etc	Aligned laser cutting to provide a highly accurate structure	The strength is not critical in this study	The effective conversion of the thermal mismatch between two closely packed constituent materials into biaxial/uniaxial thermal expansion/shrinkage via the design and fabrication of a kirigami-inspired class of 2D hierarchical metamaterials	An Ashby plot of the coefficient of thermal expansion versus density serves as a quantitative comparison of the hierarchical metamaterials	[69]
Two-photon polymerization direct laser writing	Siloxane resin system	Low density provided by SiO_xC_y	No present-day application was suggested due to the nanoscale structure	The fabrication of 3D-printed micrometer-sized pillars with features down to 200 nm in size	Under uniaxial compression, effective stiffnesses of 1–17 GPa and strengths of 40–860 MPa were obtained at relative densities of 9–40% according to the volume fraction of the solid constituent material	A significantly increased specific stiffness (i.e., ratio of stiffness to density) relative to the most advanced nano- and micro-architectured materials	Plastic behavior with a failure strain of up to 8%, despite of the presence of SiO_xC_y	[70]

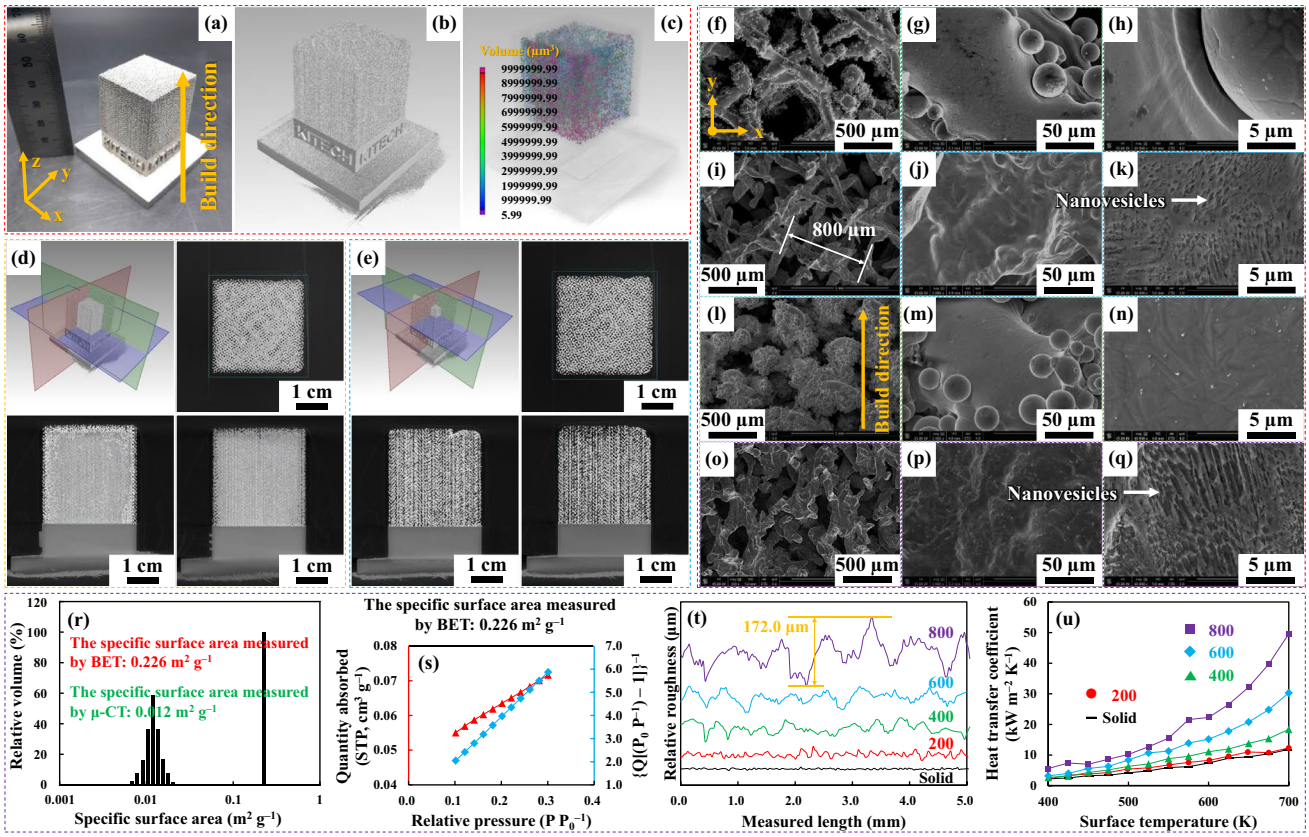

Fig. 1 **a** A photograph of the 65.1Co28.2Cr5.3Mo structure with a hatching distance of 800 μm after removing the excess powder by electrochemical leaching. **b** The μ-CT image of the lattice shows the pore-size distribution. **c** The specific surface area of the lattice measured using the μ-CT images. The core (**d**) was still slightly infilled with the powder due to less electrochemical leaching in this area, whereas the edge (**e**) was fully etched, which reveals the morphology of the nodes and arrangement of the struts. **r**, **s** The specific surface area of the lattice measured using the μ-CT images and BET analysis. **t** A comparison of the roughness testing results for the lattice structures with hatching distances of 80 (solid), 200, 400, 600, or 800 μm. **u** A comparison of the heat transfer coefficients of the lattices on the side plane. SEM images of the cellular structure at various magnifications: **f**–**k** the top plane before and after leaching, respectively, and **l**–**q** the side plane before and after leaching, respectively

conduction-dominant effect [14, 22]. Meanwhile, the heat transfer coefficient of the lattice with a hatching distance of 800 μm increased exponentially owing to heat convection along the nodes and struts, in addition to heat conduction in the material. This is because there was no contact between the lattice structure and the heat source within the vacuum environment (10^{-6} bar), although heat conduction along the ligaments of the material might influence the heat transfer coefficient a little. A random but broad distribution of nanovesicles throughout the network structure of the lattice (even covering the inside of the lattice) further increased the heat transfer coefficient. As shown in Fig. 1f–q, although the nodes were relatively sufficiently ordered, the distribution of the struts was random on the top plane, despite the continuous laser pathway, because many of them became disconnected or were missing from the main ligaments of the lattice. In the short-range order, the nodes conjugated with the struts exhibited a periodic arrangement, whereas the struts in the long-range order were disconnected and occasionally absent. This created an amorphous-inspired, glass-like structure with a disordered configuration [23–25].

3.2 Comparison of the solid and lattice microstructures

As shown in Fig. 2a, although laser irradiation accurately applied to the powder bed fabricated a lattice with a hatching distance of 800 μm over the microstructure, two distinct phases (one each in the top and side planes) were generated [7, 8]. As deduced from the specific microstructure, the heat generated by the selective laser melting process was concentrated in the nodal area because the thermal energy could not be transferred by the adjacent powder with low thermal conductivity [7–9]. Thus, the heat became concentrated and hardly flowed along the interconnected struts below, thereby forming fine equiaxial dendrites (Fig. 2b–e). By contrast, when the strut area was tightly conjugated close to the nodal area, the

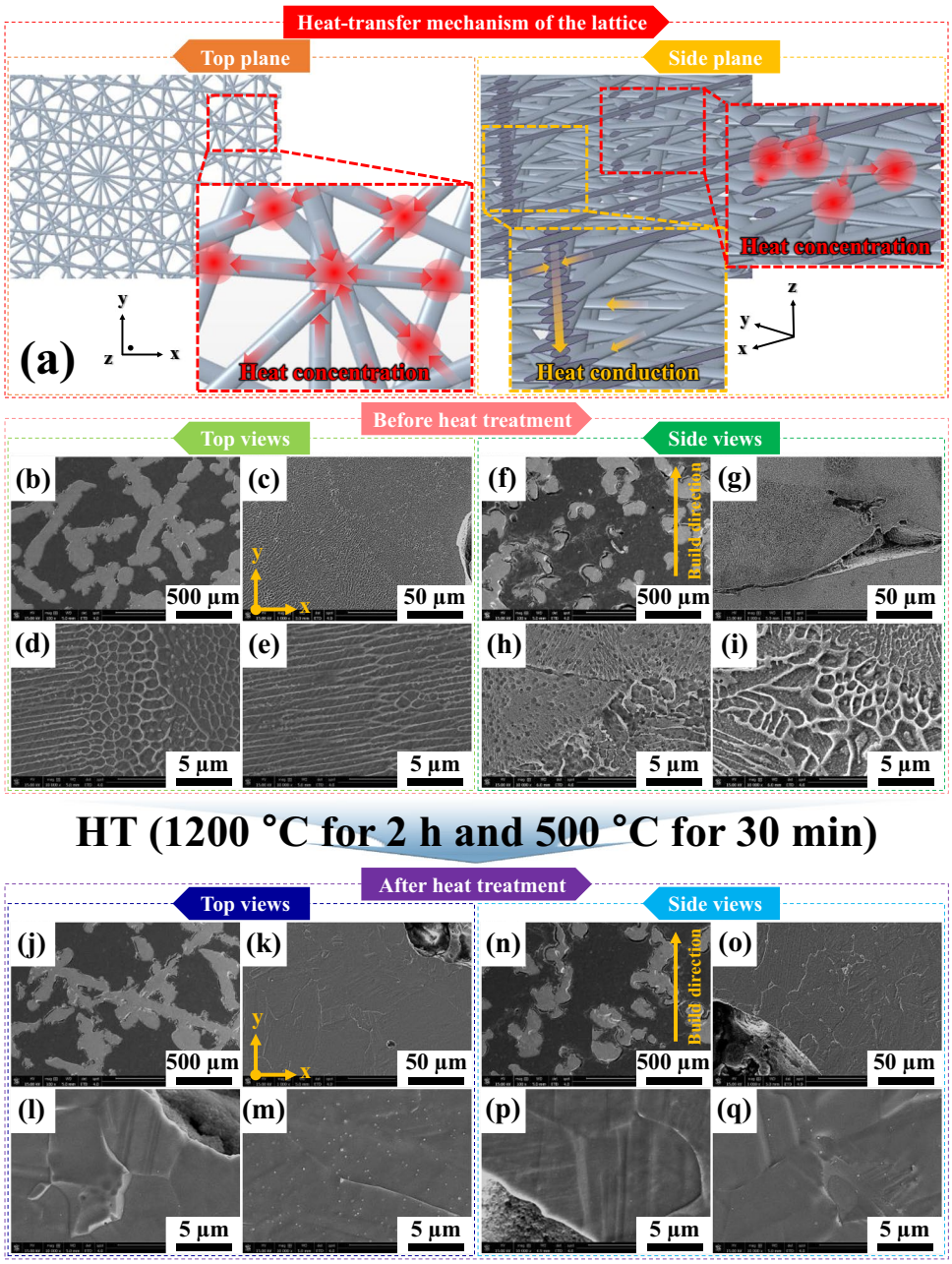

Fig. 2 **a** A schematic illustration of the heat-transfer mechanism in the as-built 65.1Co28.2Cr5.3Mo lattice additively manufactured with a hatching distance of 800 μm before HT. **b–e** The top-plane images show the formation of (i) equiaxial dendrites in the nodal area, where the thermal flow was hindered by loosely-attached regions or empty spaces, and (ii) columnar dendrites in the strut area, where the thermal energy flowed easily along the entangled longitudinal ligaments during AM. (f–i) The side-plane images show fewer acicular dendrites compared to the microstructures in the solid. **j–m** The top-plane images show that the melt pools generated by laser irradiation disappeared and were replaced by blunt-shaped columnar dendrites within distinguishable grains from the inner core to the external surface along the direction of heat extraction, irrespective of the nodal and strut areas. **n–q** The side-plane images show blunt-shaped columnar dendrites comprising only the primary γ-fcc phase

thermal energy spread throughout the highly branched ligament pathway without suppressing heat transfer, thus leading to the formation of fine columnar dendrites within the microstructure [26]. Both the columnar dendrites comprising the lighter-colored fcc phase (JCPDS No. 00–15–0806) and the equiaxial dendrites comprising the darker-colored hcp phase (JCPDS No. 01–089–4308) were present in the protuberant side plane (Fig. 2f–i) with overlapping connections to the fan-shaped melt pools [4, 5]. The thermal energy becomes concentrated at the bottom peripheral region of the cellular structure (opposite to laser irradiation) [27–29]. This led to the formation of more ε-hcp phases with unexpectedly large equiaxial dendrites, which commonly appear in the as-cast microstructure [6, 30]. This was because the thermal energy was trapped and could not be transferred when the struts were disconnected. However, when the struts were interconnected, the heat obtained from direct laser irradiation was able to flow smoothly in the upper and core regions of the cellular structure [26, 31]. Furthermore, the partial area of the ε-hcp phase transformed from the γ-fcc phase and became abundant and more stable owing to the subsequent annealing process in the lattice during repeated thermal cycling caused by continuous laser irradiation [27, 32–34]. Meanwhile, the intermetallic compounds segregated at the interfacial boundaries between the two phases were percolated in higher amounts, possibly because of their high energy states [9, 27]. At the same time,

the carbides and oxides were precipitated out at the interfacial boundaries, irrespective of whether they were in the top or side planes [9, 27]. After HT was performed to disperse the constituent elements in the lattice homogeneously, all of the melt pools disappeared from both the top (Fig. 2j–m) and side (Fig. 2n–q) planes of the microstructures. This left only the blunt-shaped columnar dendrites comprising the γ-fcc phase all over the grains. The developed directions of the columnar dendrites mostly radiated from the core to the outer surface of the lattice [6, 30]. Therefore, the thermal energy flowed along these directions and facilitated cooling [35]. In addition, the segregates and precipitates isolated at the inter-dendritic and grain boundaries (many were present in the melt pools) were dissolved owing to their active diffusion at high decomposition temperatures [35].

The grain boundary maps, phase maps, kernel average misorientation (KAM) maps, and inverse pole figure (IPF) maps corresponding to the image quality (IQ) maps of the EBSD micrographs in Fig. 3 compare the grain morphologies and growth directions, phase constituents, crystallographic distortions, and crystallographic orientations of the additively manufactured lattice structure with a hatching distance of 800 μm before and after HT. First, before HT, the low-angle grain boundaries (LAGBs; $1° < \theta < 5°$), distinct phase constituents, and distinct crystallographic distortions were revealed by the contrast-distinguished color micrographs of the lattice (Fig. 3c). In particular, the red-lined regions indicate the presence of highly dense LAGBs (2.13 cm in length within the overall length of 9.91 cm) that were mostly aligned along the grains. Based on the micrograph, the crystalline defects and microstructural abnormalities were similarly aligned along the grain boundaries and even more differentiated after identifying the γ-fcc and ε-hcp phases in the phase map (Fig. 3d) [4, 5, 14, 36, 37]. Then, the as-printed lattice was developed with the elongated grains distributed from the center to the edge of each melt pool perpendicular to the direction of laser irradiation in the IPF map (Fig. 3f). This distribution is more commonly found in the top-plane microstructure of the additively manufactured solid structure (Fig. S7f). However, bearing in mind the similarity to the crystallographic orientation of each grain in the as-printed solid structure, the grain orientations in the lattice were highly associated with the (0 0 1) and (1 1 0) planes for the γ-fcc phase in the nodes or along the struts mainly composed of the elongated grains. By contrast, in some of the nodal regions, the equiaxial grains with the preferred (0 0 0 1) plane for the ε-hcp phase were predominant, especially in the peripheral area of the lattice, wherein heat flow was prevented owing to the empty spaces or loosely attached powder with low thermal conductivity [38, 39].

Figure 4a reveals the formation of γ-fcc and ε-hcp phases with distinct interfacial boundaries in the nodal and strut areas of the lattice. Figure 4b and c show that the nanosized precipitates mainly were dispersed along the interfacial boundaries between the γ-fcc and ε-hcp phases (Fig. 4d). Figure 4g shows a high-magnification TEM image of entangled Cr,(Co,Mo), Co_3Mo_2Si, $Cr_{23}C_6$, and MoC precipitates that had accumulated at the interface between the γ-fcc and ε-hcp phases. The lattice fringe measurements in each region revealed the presence of the γ-fcc (Fig. 4k), precipitate (Fig. 4g), and ε-hcp (Fig. 4o) phases. Various spot and dot patterns were apparent from the SAED analyses performed on each phase. These corresponded to the γ-fcc phase of 65.1Co28.2Cr5.3Mo adjacent to the ε-hcp phase and segregates and precipitates with the distinct patterns, which collectively deteriorated the compression strain of the lattice [6, 30, 35, 40, 41]. In addition, EDS mapping across the interfaces was performed to evaluate the chemical compositions of the γ-fcc, precipitate, and ε-hcp phases (Fig. S8). The negative effect on the compression strength of the as-built 65.1Co28.2Cr5.3Mo lattice was primarily related to the multiple phases along the interfacial boundaries, and this effect increased the densities of voids, dislocations, and stacking faults, which additionally reduced the compression strain [8, 40, 42, 43]. Furthermore, their morphologies at the interfacial boundaries were irregular rather than smooth and spherical, thereby straightening the propagation of cracks and fractures, further reducing the mechanical strength [27]. During the highly active diffusion process generated by laser irradiation, the initially formed segregates and precipitates became isolated at the interfacial boundaries. This destabilized the microstructures in both the top and side planes due to the presence of the secondary phases [9, 27]. In terms of the solidification process, the results suggest that the interfacial boundaries could serve as favorable sites for segregation and precipitation due to their ability to stimulate nucleation. After the nucleates were formed, however, phase growth was inhibited by the uneven distributions of the segregates and precipitates at the interfacial boundaries [9, 15, 27]. Consequently, the microstructural uniformity was deteriorated, particularly at the interfacial boundaries due to (i) the formation of segregates and precipitates with differing crystallographic properties, potentially leading to residual and thermal stresses, and (ii) the negative interactions between the two neighboring (heterogeneous) phases [9, 14, 15, 27]. Thus, it significantly decreased the deformation resistance, particularly concerning the compression strain.

3.3 Compression strengths of the solid and lattice structures and determination of the optimum lattice combination by using the deep learning model

Figure 5a presents photographs of the as-built solid and lattices with hatching distances of 80, 200, 400, 600, and 800 μm, while Fig. 5b presents their respective compressive

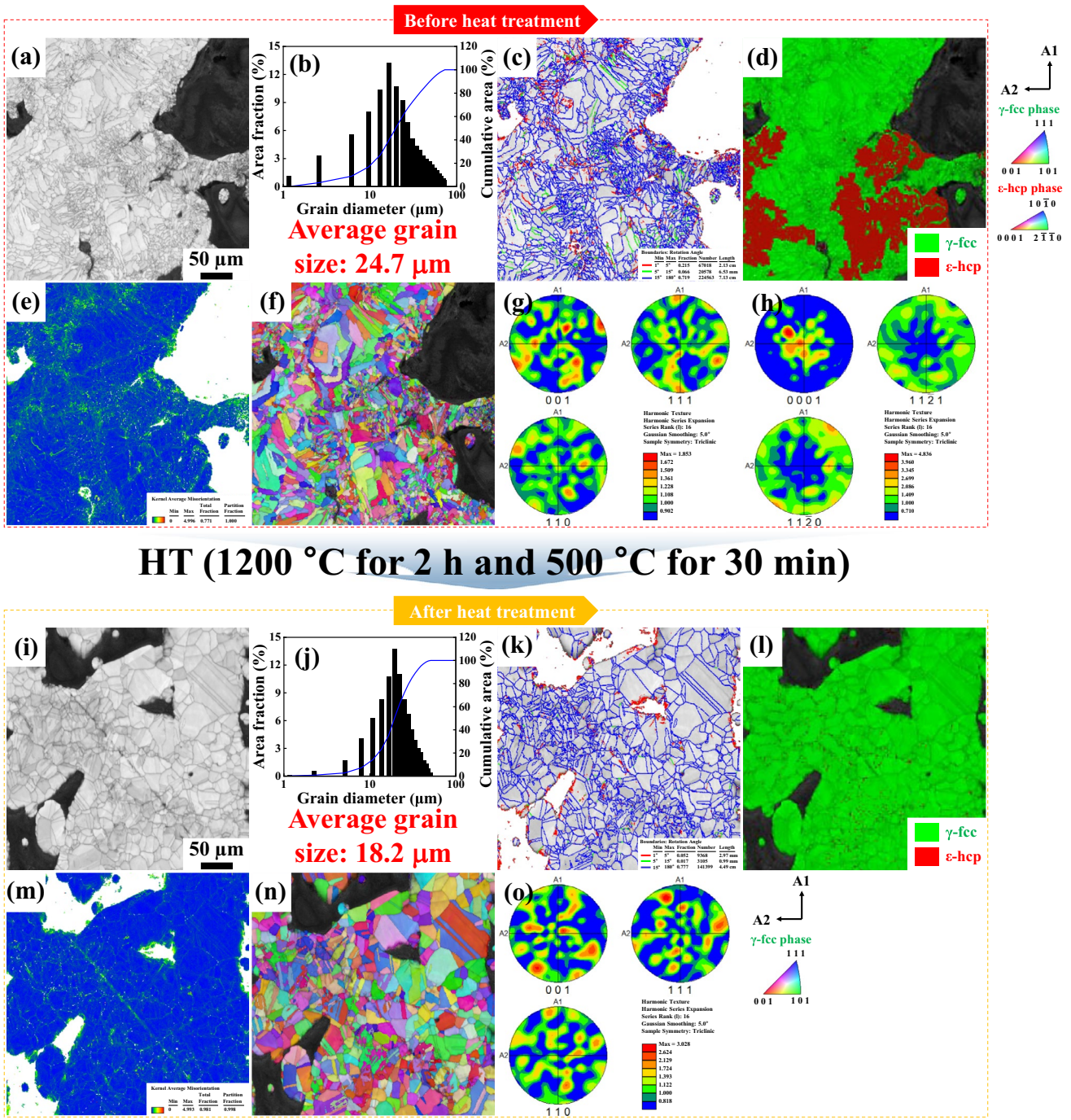

Fig. 3 **a**, **i** The IQ maps; **b**, **j** the grain size distributions; **c**, **k** the grain boundary maps (red: < 5° boundary; green: > 5° and < 15° boundaries; blue: > 15° boundary); and **d**, **l** the phase maps of the additively manufactured 65.1Co28.2Cr5.3Mo lattice structure before and after HT. **e**, **m** The KAM maps (color contrast images from blue to red according to the misorientation density); **f**, **n** the IPF maps; and **g**, **h**, and **o** the pole figures (**g** and **o** for the γ-fcc phase and **h** for the ε-hcp phase) of the hatching-distance-controlled lattice structure before and after HT

(engineering) stress–strain curves based on their relative densities (8.3, 7.7, 6.3, 3.3, and 2.3 g cm^{-3}). Compared to the standard solid with a yield strength of 895.6 MPa, all the lattices exhibited much lower values owing to vacant spaces within these structures. However, their specific yield strengths were high enough (98.2, 95.8, 92.1, and 88.5 MPa cm^3 g^{-1}, respectively) compared to the solid structure (107.9 MPa cm^3 g^{-1}). This was due to (i) their amorphous-like composition and (ii) densely distributed nodes crosslinked with highly entangled struts. It can be

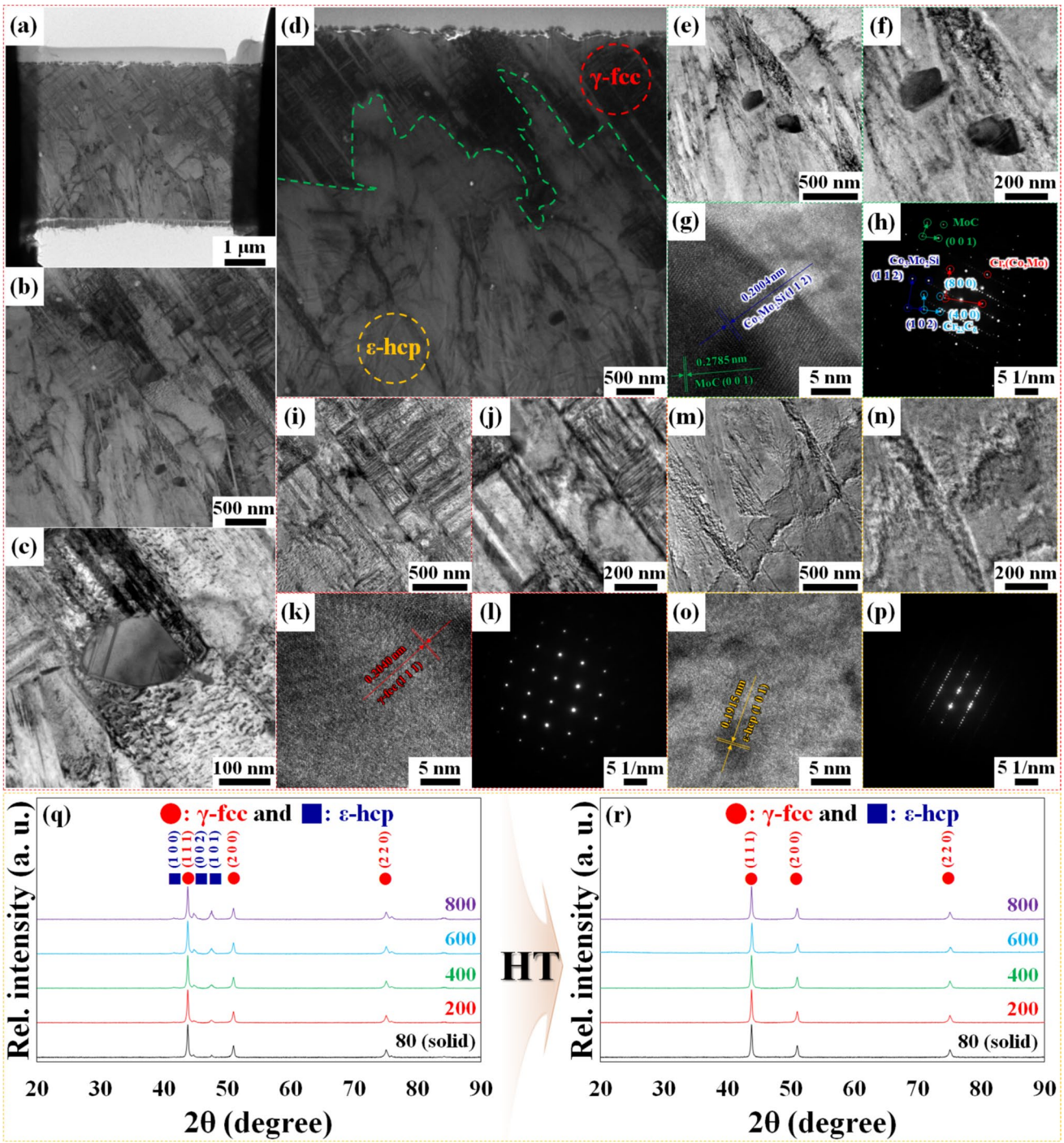

Fig. 4 **a**–**c** The TEM images of the as-built 65.1Co28.2Cr5.3Mo lattice (800 μm hatching distance) show the segregates and precipitates along the interfacial boundaries between the γ-fcc and ε-hcp phases, which significantly affected the compression strength. **d** The low-magnification; **e**–**f**, **i**–**j**, and **m**–**n** intermediate-magnification; and **g**, **k**, and **o** high-resolution TEM images with the corresponding lattice fringe measurements. **h**, **l**, and **p** The SAED patterns of (**h**) the segregates and precipitates, (**l**) primary γ-fcc phase, and (**p**) secondary ε-hcp phase. The XRD patterns of the 65.1Co28.2Cr5.3Mo structures with hatching distances of 80 (solid), 200, 400, 600, or 800 μm: **q** before HT, showing that the small amount of the secondary ε-hcp phase in the primary γ-fcc phase increased distinctively owing to greater heat condensation in the peripheral area of the disconnected melt pools (where the thermal energy could not flow easily through the powder with low heat conductivity) than in the core area; **r** after HT, indicating that the lattices with the heterogeneous phases became homogeneous, thereby suppressing the formation of the secondary phases (ε-hcp, segregates, and precipitates)

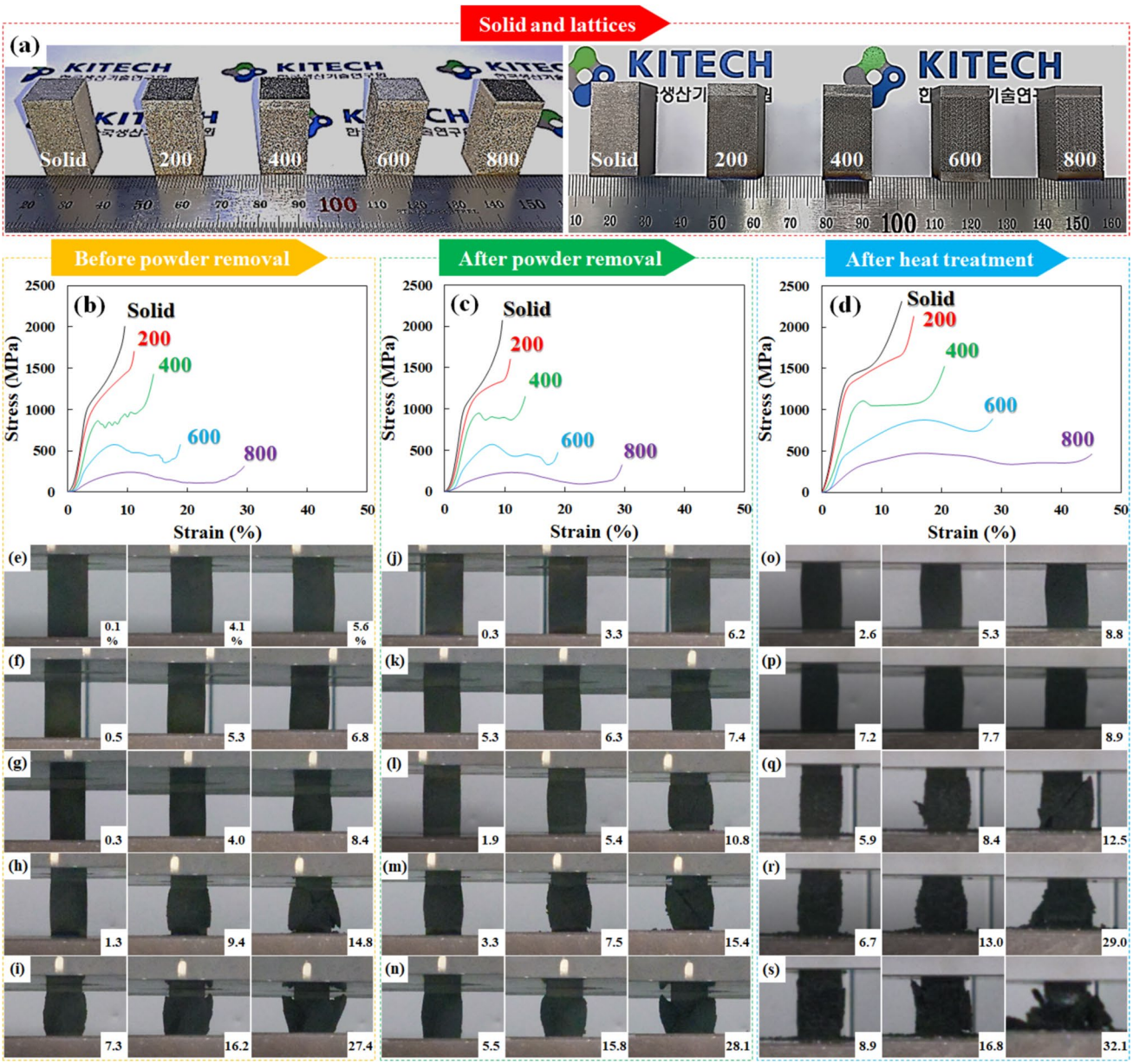

Fig. 5 **a**, **b** The compression strengths of the as-built lattices gradually decreased with increasing hatching distances because of their lower relative densities and hollower structures. However, the lattices showed unexpectedly high compression strengths owing to (i) their amorphous-like structures and (ii) the presence of highly overlapped nodes with densely aligned struts. **c** After the removal of the powder from the lattices via electrochemical leaching, the collapse was induced along the planes when the external load was applied. This may be due to the reduction in the deformation behavior of the bound powder, as indicated by considerable smoothing of the undulations in the compression testing graphs. **d** Meanwhile, the lattices had higher compression strengths after HT owing to (i) the uniform formation of only the primary γ-fcc phase, irrespective of the nodal and strut areas, and (ii) the removal of the residual and thermal stresses

concluded that the specific lattice structure is robust owing to the combination of periodically arranged nodes in the short-range order and aperiodic glass-like struts in the long-range order. In detail, the nodes played a significant role in withstanding the applied stress because they were tightly overlapped and crosslinked by the struts [44]. In addition, they tended to be uniformly aligned along the continuous laser irradiation pathway, thus displaying a crystal-like morphology. By contrast, the struts in the as-built structure were firmly but randomly connected to the adjacent nodes owing to the active diffusion initiated by laser irradiation, thus presenting a non-crystalline, glass-like morphology [44, 45]. Consequently, the impact energy was directly transferred, absorbed, and dissipated in the network structure of the lattice, leading to an increase in its mechanical strength [9]. This contrasts with the results for the conventional

structures, which rely on the constitutions and thicknesses of their struts [13, 39]. In the case of the as-built structure, however, the external pressure and force were broadly transferred by the densely distributed nodes crosslinked with the highly entangled struts [39]. These struts resisted the applied load by using their combined strength in the elastic deformation region or by resisting the impact energy through the plastic deformation region over the inner and outer grids. Therefore, the struts that were involved in the thin entangled ligaments of the as-built structure served as effective stress transmitters [46]. Instead of being distributed throughout the entire structure, the transfer of external load was partially blocked by the already disconnected struts, or by the formation of additional cracks and fractures. Thus, part of the impact energy was scattered and canceled out, thereby resulting in an unexpectedly high specific compression strength [45, 46]. Moreover, the powder existing outside and naturally inside the cellular structure was loosely attached to the ligaments during laser irradiation. Consequently, the initiation of cracks and fractures due to the back stress resulting from the accumulation of voids, dislocations, and stacking faults (i.e., the Bauschinger effect) tended to proceed randomly. This, in turn, resulted in fluctuation in the compression stress–strain curve of the cellular structure [13, 14]. Thus, removing the powder from each cellular structure using electrochemical leaching improved the specific compression strength marginally (Fig. 5c) [9, 15, 47]. Figure 5d shows the improvement in the compression strength of each cellular structure caused by HT. For example, even the lattice structure with a hatching distance of 800 μm had a yield strength and strain of 288.8 MPa and 7.3%, respectively, which were much higher than those of the as-built lattice (203.6 MPa and 6.0%) and after powder removal (224.3 MPa and 6.2%), despite having a significantly lower relative density of 2.1 g cm^{-3}. This was because HT produced the γ-fcc phase uniformly over the microstructure and alleviated the residual and thermal stresses generated by strong laser irradiation. The decrease in the grain size from 24.7 to 18.2 μm, even in the thin nodes and struts of the microporous lattice, contributed to the increased strength, consistent with the Hall–Petch effect. Annealing (HT) alleviated the residual stress in the hatching-distance-controlled lattice structure and reduced the densities and distributions of crystalline defects and microstructural abnormalities, thereby improving its compression strain.

The compression testing results for the single- or multimodal structures with 2-, 4-, or 8-lattice combinations are presented in Fig. 6, Fig. S9, and Fig. S10. Based on these results, the lattice alignment derived via deep learning was used to generate a specific lattice combination of 700/300/400/500/300/600/300 in the upper block and 300/800/300/600/300 in the lower block, along with a 1-mm-thick intercalating layer. This was aimed at achieving a compression yield strength of 300.0 MPa. During the partitioning of 8 lattices with hatching distances of 80 (solid), 200, 300, 400, 500, 600, 700, or 800 μm, their respective compression strengths emerged in the predetermined regions. Thus, the deep learning process created distinctive metastable geometric patterns based on the partitions in these regions [46, 48, 49]. By using the lattice alignment as the output, the deep learning process assigned the higher-strength lattices with lower hatching distances to the side of the upper block and the opposite side of the lower block. Then, based on the FEA of the lattice combination (Fig. S10), the upper block exhibited more partitions and, hence, more complex equivalent gradient stress was distributed along the meta-structure. The lower block could alleviate the equivalent gradient stress directly transferred from the upper block, thereby concentrating each equivalent stress in the lattices with higher hatching distances. Consequently, the equivalent stress concentration and distribution explain how the lattice combination can achieve the target compression strength. The previous compression testing results determined that a greater number of partitions decreased the yield strength of the lattice combination, whereas increasing the thickness of the intercalating layer improved the compression strength. Thus, the CNN determined that the lattices with lower hatching distances were often assigned to the upper block to achieve the required yield strength of 300.0 MPa. There were comparatively fewer partitions in the lower block. Thus, the strength of each lattice was considered more critical than that of each lattice in the upper block. The remaining lattices were assigned to support the entire structure, irrespective of whether they were in the upper or lower blocks.

We report the AI-configured metastable alignment of lattices to maintain an abnormally high specific compression strength via the integrated use of laser-irradiated lattices with high hatching distances [50–55]. The metastable alignment of the lattice combination leads to a high elastic modulus compared to the relative density. This is because the deformation mechanism is stretching-dominant rather than bending-dominant, which helps to resist the external load more effectively [45, 56–58]. Moreover, due to the relationship between $\widetilde{E} / E_s$ and $(\widetilde{\rho} / \rho_s)^n$, the as-designed metastable structure is more susceptible to the elastic modulus than is the conventional cellular structure. This is because the conventional cellular structure is dominated by the relative density, which is controlled by the strut constitution and thickness [45, 56–58]. In addition, the balance of collapse and the similarity of alignment between the lattices were considered as additional critical factors for obtaining a lattice alignment that provides a high-strength metastable structure [45, 56–58]. For example, when lattices with a hatching distance of 400 μm or less were specifically placed next to the partitions, it was better to use lattices with similar

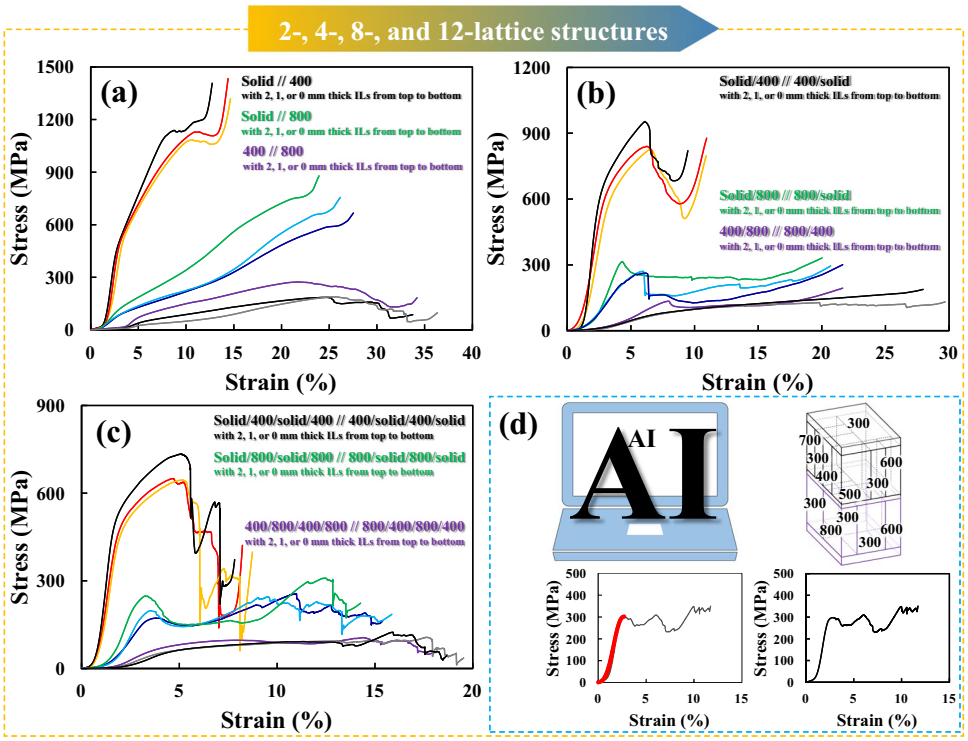

Fig. 6 Compression strength evaluations of the multi-modal lattice structures comprising **a** 2, **b** 4, or **c** 8 lattices. **d** AI was used to suggest the 12-lattice combination of 700/300/400/500/300/600/300 (7 in the upper block) and 300/800/300/600/300 (5 in the lower block), to achieve a yield strength of 300.0 MPa. FEM was used to calculate the yield strength of the meta-structure. Finally, the actual yield strength of the additively manufactured lattice combination was measured experimentally via compression testing

hatching distances on the opposite side to ensure the balance of collapse during compression testing. Furthermore, the compression testing results of the AI-augmented cellular structure with the specific lattice combination demonstrated the desired distinctive integration of highly brittle and considerably more ductile behaviors [26, 31, 39, 50–52]. Specifically, the highly brittle behavior occurred because the densely distributed nodes that were crosslinked with the highly entangled struts effectively prevented the applied load from being transmitted through the entire structure owing to the high elastic modulus compared to the relative density. Meanwhile, the considerably more ductile behavior arose due to the generation of a consistent plateau region in which the ligaments could buckle [26, 31, 39, 50–52]. These findings confirmed the modification from a fracture-dominated failure mode to a buckling-dominated failure mode, accompanied by suppression of the catastrophic failure observed in the conventional cellular structure [45, 56–58]. Overall, the compression stress–strain curve revealed a more-or-less highly elastic behavior, followed by a linear response in the plateau region, in contrast to the catastrophic fracture-dominated behavior of the conventional cellular structure [45, 56–58]. Thus, the AI-augmented metastable structure efficiently maintains its high specific compression strength and ultralight relative density without undergoing substantial degradation [26, 31, 39, 50–52, 59]. This is due to the nearly linear relationship between its elastic modulus and relative density [26, 31, 39, 50–52]. Consequently, the current study successfully designed a deep-learning-derived lattice combination that was verified by means of FEA and can potentially attain the target compression strength of 300.0 MPa under experimental compression testing. In practice, the actual compression strength of the lattice combination was 299.1 MPa, which is extremely close to the statistically

deep learned and computationally calculated compression strengths of the lattice combination.

3.4 The high-performance lattice structure additively manufactured using the deep learning model

A case study on the topological optimization of a valve cage used in a power facility was conducted in this study, as depicted in step 3 of Fig. 7. For topological optimization, we analyzed how the equivalent stress was distributed on the valve cage when the external pressure and force interacted with the part with a unique orientation while excluding any structural deformation of the planes and sheets in the top and bottom faces [13, 32, 60]. Based on this topological optimization, the geometric boundary was comparted to obtain a maximum equivalent stress of slightly less than one-third of the yield strength (416.2 MPa). This, in turn, was based on the previous compression testing of the aged 65.1Co28.2Cr5.3Mo structure that was additively manufactured along the vertical direction. Thus, the volume reduction was maximized until the safety factor was slightly higher than 3.0. From a geometrical perspective, the newly designed part sufficiently surpassed the required mechanical stiffness and deformation resistance. However, hot and cold fluids recycled inside the topologically optimized valve cage caused the accumulation of thermal stress, which undermined the part's durability and hindered fulfilment of the power facility's high safety requirement. As depicted in step 4 of Fig. 7, the thermal energy gradient distribution of the topologically optimized valve cage according to the hot fluid flow differed for each component. The top plate was less

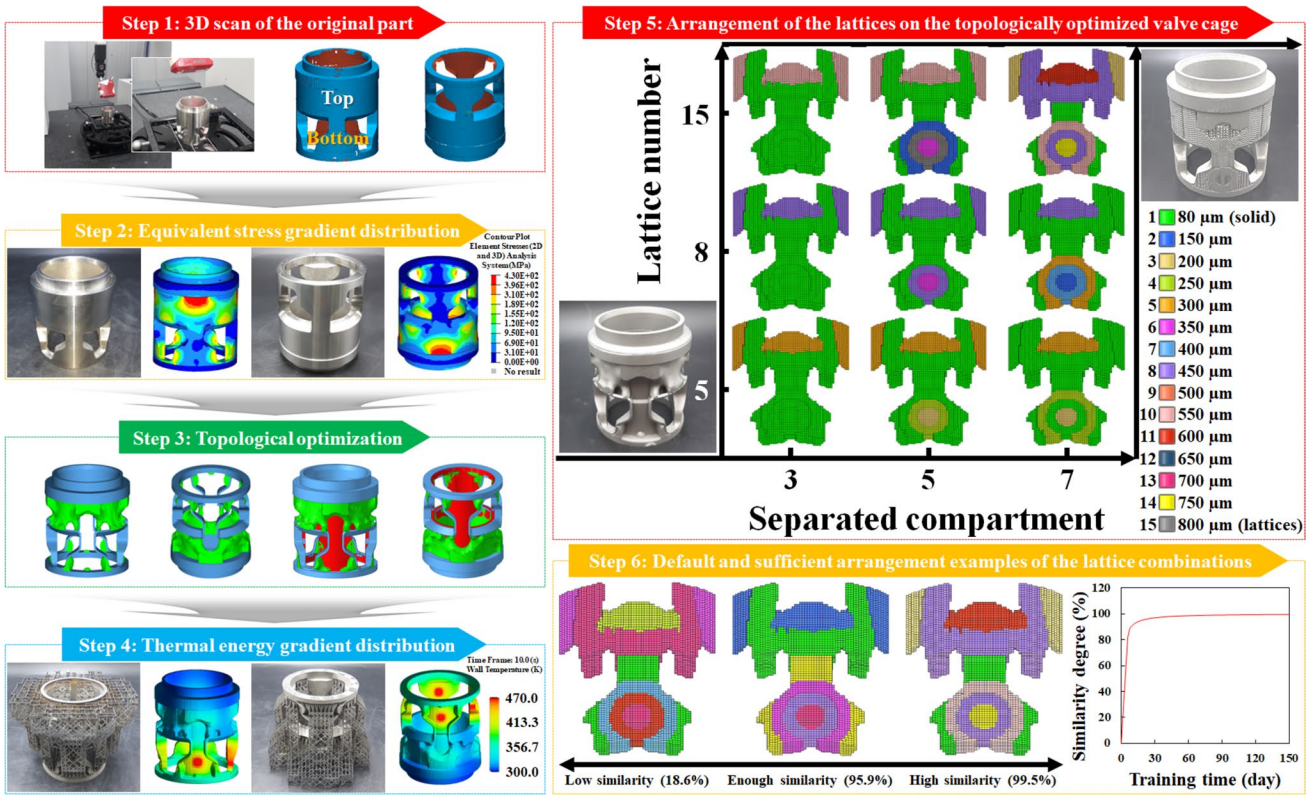

Fig. 7 Step 1: Photographs and schematics of the original part before topological optimization. Step 2: The equivalent stress gradient distribution in the original part under the applied pressure (3 MPa) and force (5000 N) to verify the solid deposition and space removal during AM. Step 3: Topological optimization to maximize the stiffness and minimize the weight of the part so that it can bear the maximum equivalent stress of 410.0 MPa (close to one-third of the yield strength (416.2 MPa) for the aged 65.1Co28.2Cr5.3Mo solid additively manufactured along the vertical direction) while reducing its weight by more than 43%. Step 4: The residual and thermal stresses caused during the recycling of hot and cold fluids become concentrated and accumulated on the main components of the valve cage. Thus, to effectively dissipate the residual heat out to the valve cage, maximize the heat exchange effect, and lower the heat accumulation, the previously designed lattice structures with various hatching distances were attached to the outer plate of the topologically optimized part. Step 5: Three lattice combinations with various hatching distances (5 lattices: 80 (solid), 200, 400, 600, and 800 μm; 8 lattices: 80 (solid), 200, 300, 400, 500, 600, 700, and 800 μm; and 15 lattices: 80 (solid), 150, 200, 250, 300, 350, 400, 450, 500, 550, 600, 650, 700, 750, and 800 μm) were arranged on three separate compartments (3, 5, and 7) with an identical number of elements (18,412) on the outer plate of the topologically optimized valve cage based on attaining a high compression strength and large surface area in the combined ratio of 50%: 50% of their maxima by using deep learning

thermally stressed because the hot fluid only passed through the fluid-flow passages, and the stem piston obstructed the fluid flow. By contrast, on the bottom plate, the thermal stress was mainly concentrated between the fluid-flow passages. Thus, it is better to use lattices with lower hatching distances in the regions with lower thermal stress because thermal conductivity predominates over heat convection in these lattices. The bottom-plate regions subjected to higher thermal stress due to the hot fluid flow under the stem piston required lattices with higher hatching distances of up to 800 μm. In this way, the thermal stress could be alleviated more rapidly by draining the generated thermal energy via the lattices with larger surface areas. After combining the structural and thermal stress gradient distributions, the top plate required denser lattices, whereas the bottom plate required sparser lattices.

Figure 7 (steps 5 and 6) illustrates various combinations of lattice structures according to the numbers of separated compartments and lattices. Each compartment can construct these structures differently to achieve maximum mechanical stiffness and thermal release performances. As shown, the use of a combination of 15 lattices (80 (solid), 150, 200, 250, 300, 350, 400, 450, 500, 550, 600, 650, 700, 750, and 800 μm) for all 7 compartments in the topologically optimized part maximized its heat-exchange capability. Meanwhile, a combination of 5 lattice structures (80 (solid), 200, 400, 600, and 800 μm) in 3 compartments (2 compartments in the top plate and 1 compartment in the bottom plate) took the least time to construct. As determined by using the CNN, the part with the fewest lattices in each separate compartment required a combination of lattices with lower hatching distances, including the solid (80 μm). However, the resulting heat extraction performance was poorer than that achieved by using a combination of lattice structures with higher hatching distances [48, 49]. Thus, although the valve-cage part that was constructed using mainly the solid was structurally stable, it was more vulnerable to the accumulation of thermal stress. The output from the CNN indicated using the lattice with a hatching distance of 400 μm only when the ratio between the equivalent and thermal stresses was set to 50%: 50% of their maxima. This selection imparted structural stability and thermal steadiness; the results were similar even in the cases of 100% equivalent stress or 100% thermal stress. Although the CNN recognized these factors, it presented only one of the many possible lattice combinations. For example, when the part was required to be established using 7 compartments and 15 lattices to achieve the expected results, it included the highest thermal energy-dissipation area that matched the lattice with a hatching distance of 750 μm. However, this was smaller than that of the lattice with a hatching distance of 800 μm when considering only the thermal energy extraction. Thus, the lattice with a hatching distance of 750 μm was suggested because of the structural stability requirement. Meanwhile, each boundary (referred to as a compartment herein) within which the cellular structure was applied satisfied the continuity requirement by connecting to the thin intercalating layer of 160 μm, which allowed for the smooth transfer of load between the compartments [9]. However, the heat extraction capability deteriorated because of the intercalating layer, which improved the structural stability relative to its thickness and vice versa. In addition, the analysis time for identifying the effective alignment among the lattice combinations was influenced by the numbers of separated compartments and lattices. The longer-aligned lattice combinations provided more accurate alignments of the cellular structures (step 6 of Fig. 7). In principle, it is better to obtain highly precise alignment data, especially for the parts used in a power facility, which require high durability and safety, irrespective of the time needed for the analysis. However, the composition of the training dataset used to complete the analysis took several tens or hundreds of days. Fortunately, only 10 days were required to reach a sufficient alignment (validation) accuracy of 95.9% compared to an analysis time of 150 days for an accuracy of 99.5%. Furthermore, the lattice alignment was highly accurate and reasonably intuitive. For example, the circular region in the bottom plate matched the lattice with a hatching distance of 700 μm with a validation accuracy of 95.9%, compared to 99.5% when using the lattice with a hatching distance of 750 μm. However, the lower analysis time had an accuracy of only 18.6% after 3 days. This yielded a poor lattice alignment that degraded both the stiffness and heat extraction performance. Moreover, the resulting performance was weaker even than that obtained via topological optimization only. Consequently, by combining the lattices with various hatching distances in pairs with the most widely spaced compartments aligned on the outer plate of the topologically optimized valve cage, we were able to maximize the mechanical stiffness (minimize the structural deformation). At the same time, we were able to provide effective heat extraction, thereby reducing the damage caused by fatigue and stress in the valve cage. Hence, the efficient lattice alignment computed using the CNN can provide an evolutionary pathway for the design for additive manufacturing (DfAM) of a valve cage for use in a power facility, thus leading to the optimum performance levels in terms of mechanical stiffness and surface area [61–64].

4 Conclusion

Regarding the deep-learning-augmented DfAM, various hatching-distance-controlled lattices with nanometer-scale vesicles generated by electrochemical leaching on the surfaces of micrometer-scale nodes and struts via the LPBF

process were aligned to obtain a high mechanical stiffness and large surface area (50% of each maximum) on the outer plate of the valve cage. Upon retention of the unexpectedly high specific compression strengths, these novel lattices were characterized by the amorphous-inspired structure with periodic and aperiodic arrangements in the short- and long-range orders, respectively, and the presence of densely distributed nodes and highly entangled struts. Their microporous and nanovesicular structures can broadly and rapidly emit the thermal energy to the outside of the lattice combination to prevent heat accumulation (concerning the thermal safety) of the part mainly used in the power facility. In addition to removing the powder to reduce the deformation behavior and induce the smooth transfer of load during compression testing, adding an intercalating layer between the lattices prevented mutual propagation between the lattices after each breakage by absorbing the deformation energy according to its thickness. As such, the AI successfully configured the metastable alignments of the amorphous-inspired lattices. Based on this approach, a more advanced valve cage was fabricated by following all the tenets of AM from A through Z to check the possibility of using it in a practical (even commercial) power plant.

Supplementary Information The online version contains supplementary material available at https://doi.org/10.1007/s42114-024-01039-6.

Acknowledgements We express our sincere gratitude to all those authors who have been associated with this assignment and have made it a worthwhile experience.

Author contributions Seong Je Park and Woongbeom Heogh contributed equally to this work and wrote and edited the paper. Jeongho Yang, Sukhyun Kang, Wonjong Jeong, and Hoyoung Lee additively manufactured the solid and lattice structures. Seung Chul Han, Young Won Kim, and Xingyu Fu helped analyze the structures using microscopic and spectroscopic techniques and measuring the mechanical properties. Tae-Sik Jang, Hyun-Do Jung, Mohammad Jahazi, Hyoung Seop Kim, Myoung-Gyu Lee, Susmita Bose, Amit Bandyopadhyay, Martin Byung-Guk Jun, Rigoberto C. Advincula, Clodualdo Aranas Jr., and Sang Hoon Kim contributed to the interpretation and discussion of the experimental results.

Funding This work was supported by a New Faculty Research Grant of Pusan National University, 2024. In addition, this work was supported by the National Research Foundation of Korea (NRF) grant funded by the Korean government (MSIP) (NRF-2021R1A2C3006662, NRF-2022R1A5A1030054, and RS-2024-00405381). The authors acknowledge the support of the Natural Sciences and Engineering Research Council of Canada (NSERC), Canada Foundation for Innovation (CFI), Atlantic Canada Opportunities Agency (ACOA), and New Brunswick Innovation Foundation (NBIF).

Data availability This manuscript has been published as open access.

Declarations

Competing interests The authors declare no competing interests.

References

1. Gu D, Shi X, Poprawe R, Bourell DL, Setchi R, Zhu J (2021) Material-structure-performance integrated laser-metal additive manufacturing. Science 372:eabg1487
2. Zheng X, Smith W, Jackson J, Moran B, Cui H, Chen D, Ye J, Fang N, Rodriguez N, Weisgraber T, Spadaccini CM (2016) Multiscale metallic metamaterials. Nat Mater 15:1100–1106
3. Chen L, Lan C, Xu B, Bi K (2021) Progress on material characterization methods under big data environment. Adv Compos Hybrid Mater 4:235–247
4. Sun SH, Koizumi Y, Kurosu S, Li YP, Chiba A (2015) Phase and grain size inhomogeneity and their influences on creep behavior of Co–Cr–Mo alloy additive manufactured by electron beam melting. Acta Mater 86:305–318
5. Sun SH, Koizumi Y, Kurosu S, Li YP, Matsumoto H, Chiba A (2014) Build direction dependence of microstructure and high-temperature tensile property of Co–Cr–Mo alloy fabricated by electron beam melting. Acta Mater 64:154–168
6. Wei D, Anniyaer A, Koizumi Y, Aoyagi K, Nagasako M, Kato H, Chiba A (2019) On microstructural homogenization and mechanical properties optimization of biomedical Co–Cr–Mo alloy additively manufactured by using electron beam melting. Addit Manuf 28:215–227
7. Wang YM, Voisin T, McKeown JT, Ye J, Calta NP, Li Z, Zeng Z, Zhang Y, Chen W, Roehling TT, Ott RT, Santala MK, Depond PJ, Matthews MJ, Hamza AV, Zhu T (2018) Additively manufactured hierarchical stainless steels with high strength and ductility. Nat Mater 17:63–71
8. Sanaei N, Fatemi A (2021) Defects in additive manufactured metals and their effect on fatigue performance: a state-of-the-art review. Prog Mater Sci 117:100724
9. Pham MS, Liu C, Todd I, Lertthanasarn J (2019) Damage-tolerant architected materials inspired by crystal microstructure. Nature 565:305–311
10. Saccone MA, Gallivan RA, Narita K, Yee DW, Greer JR (2022) Additive manufacturing of micro-architected metals via hydrogel infusion. Nature 612:685–690
11. Clarke AJ (2022) Unusual microstructures by 3D printing. Nat Mater 21:1223–1224
12. Wang Y, Peng X, Fallatah AM, Qin H, Zhao W, Zaki ZI, Xu H, Liu B, Mao H, El-Bahy ZM, Algadi H, Wang C (2023) High-entropy CoCrFeMnNi alloy/aluminide-laminated composites with enhanced quasi-static bending and dynamic compression properties. Adv Compos Hybrid Mater 6:201
13. du Plessis A, Razavi SMJ, Benedetti M, Murchio S, Leary M, Watson M, Bhate D, Berto F (2022) Properties and applications

of additively manufactured metallic cellular materials: a review. Prog Mater Sci 125:100918
14. Sing SL, Huang S, Goh GD, Goh GL, Tey CF, Tan JHK, Yeong WY (2021) Emerging metallic systems for additive manufacturing: in-situ alloying and multi-metal processing in laser powder bed fusion. Prog Mater Sci 119:100795
15. Zerbst U, Bruno G, Buffière JY, Wegener T, Niendorf T, Wu T, Zhang X, Kashaev N, Meneghetti G, Hrabe N, Madia M, Werner T, Hilgenberg K, Koukolíková M, Procházka R, Džugan J, Möller B, Beretta S, Evans A, Wagener R, Schnabel K (2021) Damage tolerant design of additively manufactured metallic components subjected to cyclic loading: State of the art and challenges. Prog Mater Sci 121:100786
16. Hou C, Yang W, Kimura H, Xie X, Zhang X, Sun X, Yu Z, Yang X, Zhang Y, Wang B, Bin XuB, Sridhar D, Algadi H, Guo Z, Du W (2023) Boosted lithium storage performance by local build-in electric field derived by oxygen vacancies in 3D holey N-doped carbon structure decorated with molybdenum dioxide. J Mater Sci Technol 142:185–195
17. Li F, Li Q, Kimura H, Xie X, Zhang X, Wu N, Sun X, Bin XuB, Algadi H, Pashameah RA, Alanazi AK, Alzahrani E, Li H, Du W, Guo Z, Hou C (2023) Morphology controllable urchin-shaped bimetallic nickel-cobalt oxide/carbon composites with enhanced electromagnetic wave absorption performance. J Mater Sci Technol 148:250–259
18. Li Z, Han Z, Jaya D, Kumar P, Ren J, Hou H, El-Bahy ZM, Mersal GAM, Bin XuB, Liu Y, Liu C, Ibrahim MM (2023) Boron nitride whiskers and nano alumina synergistically enhancing the vertical thermal conductivity of epoxy-cellulose aerogel nanocomposites. Adv Compos Hybrid Mater 6:224
19. Wang Z, Wu Z, AlMasoud N, Weng L, Alomar TS, El-Bahy ZM, He M, Yang C, Sun M, Wasnik P, Li H, Algadi H, Annamareddy SHK, Sridhar D (2023) Effective three-dimensional thermal conductivity networks in polystyrene/multi-walled carbon nanotubes/aluminum oxide@hexagonal boron nitride composites based on synergistic effects and isolated structures. Adv Compos Hybrid Mater 6:125
20. Liu X, Lv X, Tian Q, AlMasoud N, Xu Y, Alomar TS, El-Bahy ZM, Li J, Algadi H, Roymahapatra G, Ding T, Guo J, Li X (2023) Silica binary hybrid particles based on reduced graphene oxide for natural rubber composites with enhanced thermal conductivity and mechanical properties. Adv Compos Hybrid Mater 6:141
21. Pan D, Yang G, Abo-Dief HM, Dong J, Su F, Liu C, Li Y, Bin XuB, Murugadoss V, Naik N, El-Bahy SM, El-Bahy ZM, Huang M, Guo Z (2022) Vertically aligned silicon carbide nanowires/boron nitride cellulose aerogel networks enhanced thermal conductivity and electromagnetic absorbing of epoxy composites. NanoMicro Lett 14:118
22. Wilms MB, Rittinghaus SK, Goßling M, Gökce B (2023) Additive manufacturing of oxide-dispersion strengthened alloys: materials, synthesis and manufacturing. Prog Mater Sci 133:101049
23. Fan G, Wang Z, Ren H, Liu Y, Fan R (2021) Dielectric dispersion of copper/rutile cermets: dielectric resonance, relaxation, and plasma oscillation. Scr Mater 190:1–6
24. Fan G, Wang Z, Sun K, Liu Y, Fan R (2021) Doped ceramics of indium oxides for negative permittivity materials in MHz-kHz frequency regions. J Mater Sci Technol 61:125–131
25. Xie P, Zhang Z, Liu K, Qian L, Dang F, Liu Y, Fan R, Wang X, Dou S (2017) C/SiO_2 meta-composite: overcoming the λ/a relationship limitation in metamaterials. Carbon 125:1–8
26. Tancogne-Dejean T, Spierings AB, Mohr D (2016) Additively-manufactured metallic micro-lattice materials for high specific energy absorption under static and dynamic loading. Acta Mater 116:14–28
27. Kim SH, Lee H, Yeon SM, Aranas C, Choi K, Yoon J, Yang SW, Lee H (2021) Selective compositional range exclusion via directed energy deposition to produce a defect-free Inconel 718/SS 316L functionally graded material. Addit Manuf 47:102288
28. Tian Y, Chadha K, Kim SH, Aranas C (2021) Strengthening mechanisms in a heatvar hot work tool steel fabricated by laser powder bed fusion. Mater Sci Eng A 805:140801
29. Eo DR, Chung SG, Jeon JM, Cho JW (2021) Melt pool oxidation and reduction in powder bed fusion. Addit Manuf 41:101982
30. Aota S, Yamanaka K, Mori M, Sasaki N, Adrien J, Maire E, Fabrègue D, Chiba A (2022) Solidification behavior and porosity in electron-beam powder bed fusion of Co–Cr–Mo alloys: effect of carbon concentrations. Addit Manuf 59:103134
31. Benedetti M, du Plessis A, Ritchie RO, Dallago M, Razavi N, Berto F (2021) Architected cellular materials: a review on their mechanical properties towards fatigue-tolerant design and fabrication. Mater Sci Eng R 144:100606
32. Kim SH, Yeon SM, Lee JH, Kim YW, Lee H, Park J, Lee NK, Choi JP, Aranas C, Lee YJ, An S, Choi K, Son Y (2020) Additive manufacturing of a shift block via laser powder bed fusion: the simultaneous utilisation of optimised topology and a lattice structure. Virtual Phys Prototyp 15:460–480
33. Zhang Z, Hou H, Zhang Y, Sayed MEE, Murshed MN, Samir A, Wu P, Gong C, Yong H, Song G, Fang D, Sridhar D, Algadi H, Liu B (2023) Effect of calcium addition on the microstructure, mechanical properties, and corrosion behavior of AZ61–Nd alloy. Adv Compos Hybrid Mater 6:50
34. Liu W, Liu B, Zhang S, Lin Z, Zhang Y, Wu P, Algadi H (2023) Microstructure and mechanical properties of extruded Mg–6Al–2X (X = Cu/Ni/Fe) alloy used degradable bridge plugs. Adv Compos Hybrid Mater 6:181
35. Stinville JC, Charpagne MA, Cervellon A, Hemery S, Wang F, Callahan PG, Valle V, Pollock TM (2022) On the origins of fatigue strength in crystalline metallic materials. Science 377:1065–1071
36. Zhang C, Ouyang D, Pauly S, Liu L (2021) 3D printing of bulk metallic glasses. Mater Sci Eng R 145:100625
37. Li F, Wu N, Kimura H, Wang Y, Bin XuB, Wang D, Li Y, Algadi H, Guo Z, Du W, Hou C (2023) Initiating binary metal oxides microcubes electromagnetic wave absorber toward ultrabroad absorption bandwidth through interfacial and defects modulation. NanoMicro Lett 15:220
38. Liu G, Zhang X, Chen X, He Y, Cheng L, Huo M, Yin J, Hao F, Chen S, Wang P, Yi S, Wan L, Mao Z, Chen Z, Wang X, Cao Z, Lu J (2021) Additive manufacturing of structural materials. Mater Sci Eng R 145:100648
39. Chen LY, Liang SX, Liu Y, Zhang LC (2021) Additive manufacturing of metallic lattice structures: unconstrained design, accurate fabrication, fascinated performances, and challenges. Mater Sci Eng R 146:100648
40. Hou H, Simsek E, Ma T, Johnson NS, Qian S, Cissé C, Stasak D, Al HN, Zhou L, Hwang Y, Radermacher R, Levitas VI, Kramer MJ, Zaeem MA, Stebner AP, Ott RT, Cui J, Takeuchi I (2019) Fatigue-resistant high-performance elastocaloric materials made by additive manufacturing. Science 366:1116–1121
41. Hindi J, Murthy AA, Muralishwara K, Kasipandian K, Gurumurthy BM, Naik N (2023) Tribological characterization of precipitation hardened 7075 aluminium alloy composites reinforced with cast iron particle. ES Mater Manuf 22:1034
42. Ashok A, Desai AS, Mahadeva R, Patole SP, Pandey B, Bhagat N (2023) Research network analysis and machine learning modeling on heusler alloys. Eng Sci 25:954
43. Riccio A, Sellitto A, Caraviello A, Riccio U, Torluccio A, Pacini L, Mohr R (2023) On the development of a passive shape memory alloy - based cooling system – part II: design justification. Eng Sci 25:928

44. Wang Y, Li L, Hofmann D, Andrade JE, Daraio C (2021) Structured fabrics with tunable mechanical properties. Nature 596:238–243
45. Xu X, Zhang Q, Hao M, Hu Y, Lin Z, Peng L, Wang T, Ren X, Wang C, Zhao Z, Wan C, Fei H, Wang L, Zhu J, Sun H, Chen W, Du T, Deng B, Cheng GJ, Shakir I, Dames C, Fisher TS, Zhang X, Li H, Huang Y, Duan X (2019) Double-negative-index ceramic aerogels for thermal superinsulation. Science 363:723–727
46. Zheng X, Lee H, Weisgraber TH, Shusteff M, DeOtte J, Duoss EB, Kuntz JD, Biener MM, Ge Q, Jackson JA, Kucheyev SO, Fang NX, Spadaccini CM (2014) Ultralight, ultrastiff mechanical metamaterials. Science 344:1373–1377
47. Shetty T, Pai BJ, Naik N, Samrot AV, Bhat P, Salmataj SA (2023) Protection of magnesium AZ31B alloy in a hydrochloric acid medium using gelatin and optimizing the results through response surface methodology. ES Mater Manuf 22:1066
48. DebRoy T, Mukherjee T, Wei HL, Elmer JW, Milewski JO (2021) Metallurgy, mechanistic models and machine learning in metal printing. Nat Rev Mater 6:48–68
49. Zhu Z, Ng DWH, Park HS, McAlpine MC (2021) 3D-printed multifunctional materials enabled by artificial-intelligence-assisted fabrication technologies. Nat Rev Mater 6:27–47
50. Huang EW, Lee WJ, Singh SS, Kumar P, Lee CY, Lam TN, Chin HH, Lin BH, Liaw PK (2022) Machine-learning and high-throughput studies for high-entropy materials. Mater Sci Eng R 147:100645
51. Mirhoseini A, Goldie A, Yazgan M, Jiang JW, Songhori E, Wang S, Lee YJ, Johnson E, Pathak O, Nazi A, Pak J, Tong A, Srinivasa K, Hang W, Tuncer E, Le QV, Laudon J, Ho R, Carpenter R, Dean J (2021) A graph placement methodology for fast chip design. Nature 594:207–212
52. Gu GX, Chen CT, Richmond DJ, Buehler MJ (2018) Bioinspired hierarchical composite design using machine learning: simulation, additive manufacturing, and experiment. Mater Horiz 5:939–945
53. Modi A, Kishore B, Shetty DK, Sharma VP, Ibrahim S, Hunain R, Usman N, Nayak SG, Kumar S, Paul R (2022) Role of artificial intelligence in detecting colonic polyps during intestinal endoscopy. Eng Sci 20:25–33
54. Bunian S, Al-Ebrahim MA, Nour AA (2024) Role and applications of artificial intelligence and machine learning in manufacturing engineering: a review. Eng Sci 29:1088
55. Shukla VK, Sudhi M, Shetty DK, Banthia S, Chandrasekar P, Naik N, Hameed BMZ, Girisha S, Balakrishnan JM (2023) Transforming disease diagnosis and management: a comprehensive review of AI-driven urine analysis in clinical medicine. Eng Sci 26:1009
56. Han SC, Kang DS, Kang K (2019) Two nature-mimicking auxetic materials with potential for high energy absorption. Mater Today 26:30–39
57. Han SC, Kang K (2019) Another stretching-dominated microarchitectured material, shellular. Mater Today 31:31–38
58. Surjadi JU, Lu Y (2022) Design criteria for tough metamaterials. Nat Mater 21:272–274
59. Hao D, Chen T, Guo P, Liu D, Wang X, Huang H, Huang J, Shan F, Yang Z (2023) Artificial optoelectronic synaptic devices based on vertical organic field-effect transistors with low energy consumption. Adv Compos Hybrid Mater 6:129
60. Bandyopadhyay A, Traxel KD, Bose S (2021) Nature-inspired materials and structures using 3D printing. Mater Sci Eng R 145:100609
61. Carrozza A, Cabrini M, Lorenzi S, Lombardi M, Pastore T (2023) Improving the corrosion performance of LPBF- and EBM-processed Ti–6Al–4V by chemical pickling. Eng Sci 26:985
62. Colorado HA, Gutierrez-Velasquez EI, Gil LD, de Camargo IL (2024) Exploring the advantages and applications of nanocomposites produced via vat photopolymerization in additive manufacturing: a review. Adv Compos Hybrid Mater 7:1
63. Jambhulkar S, Ravichandran D, Thippanna V, Patil D, Song K (2023) A multimaterial 3D printing-assisted micropatterning for heat dissipation applications. Adv Compos Hybrid Mater 6:93
64. Wang H, Feng W, Liu D, Zhang G, Liu Y, Wang J, Zou L (2023) Iron-based soft magnetic materials fabricated by laser additive manufacturing. Eng Sci 22:809
65. Schaedler TA, Jacobsen AJ, Torrents A, Sorensen AE, Lian J, Greer JR, Valdevit L, Carter WB (2011) Ultralight metallic microlattices. Science 334:962–965
66. Han SC, Lee JW, Kang K (2015) A new type of low density material: shellular. Adv Mater 27:5506–5511
67. Deng B, Zareei A, Ding X, Weaver JC, Rycroft CH, Bertoldi K (2022) Inverse design of mechanical metamaterials with target nonlinear response via a neural accelerated evolution strategy. Adv Mater 34:2206238
68. Guo X, Ni X, Li J, Zhang H, Zhang F, Yu H, Wu J, Bai Y, Ho L, Huang Y, Rogers JA, Zhang Y (2021) Designing mechanical metamaterials with kirigami-inspired, hierarchical constructions for giant positive and negative thermal expansion. Adv Mater 33:2004919
69. Bauer J, Kraus JA, Crook C, Rimoli JJ, Valdevit L (2021) Tensegrity metamaterials: toward failure-resistant engineering systems through delocalized deformation. Adv Mater 33:2005647
70. Bauer J, Crook C, Izard AG, Eckel ZC, Ruvalcaba N, Schaedler TA, Valdevit L (2019) Additive manufacturing of ductile, ultrastrong polymer-derived nanoceramics. Matter 1:1547–1556

Authors and Affiliations

Seong Je Park[1] · Woongbeom Heogh[2] · Jeongho Yang[3] · Sukhyun Kang[4] · Wonjong Jeong[5] · Hoyoung Lee[6] · Tae-Sik Jang[7] · Hyun-Do Jung[8] · Mohammad Jahazi[9] · Seung Chul Han[10] · Hyoung Seop Kim[11,12,13] · Myoung-Gyu Lee[6] · Susmita Bose[14] · Amit Bandyopadhyay[14] · Martin Byung-Guk Jun[15] · Young Won Kim[15] · Xingyu Fu[15] · Rigoberto C. Advincula[16,17,18] · Clodualdo Aranas Jr.[19] · Sang Hoon Kim[20]

✉ Clodualdo Aranas Jr.
clod.aranas@unb.ca

✉ Sang Hoon Kim
sanghooni791@naver.com

[1] School of Mechanical and Aerospace Engineering, Nanyang Technological University, Singapore 639798, Singapore

[2] Satellite System 5 Team, Hanwha Systems, Yongin, Gyeonggi-do 17121, Republic of Korea

[3] School of Mechanical Engineering, Pusan National University, Busan 46241, Republic of Korea

[4] Process Research 3 Team, LG Display Co., Ltd., Paju, Gyeonggi-do 10845, Republic of Korea

[5] Department of Nuclear and Quantum Engineering, Korea Advanced Institute of Science and Technology, Daejeon 34141, Republic of Korea

[6] Department of Materials Science and Engineering & RIAM, Seoul National University, Seoul 08826, Republic of Korea

[7] School of Biomedical Convergence Engineering, Pusan National University, Yangsan, Gyeongsangbuk-do 50612, Republic of Korea

[8] Division of Materials Science and Engineering, Hanyang University, Seoul 04763, Republic of Korea

[9] Department of Mechanical Engineering, École de Technologie Supérieure, Montreal, QC H3C 1K3, Canada

[10] Material & Component Convergence R&D Center, Korea Construction Equipment Technology Institute, Gunsan, Jeollabuk-do 54002, Republic of Korea

[11] Graduate Institute of Ferrous and Eco Materials Technology, Pohang University of Science and Technology, Pohang, Gyeongsangbuk-do 37673, Republic of Korea

[12] Advanced Institute for Materials Research, Tohoku University, Sendai 980–8577, Japan

[13] Institute for Convergence Research and Education in Advanced Technology, Yonsei University, Seoul 03722, Republic of Korea

[14] School of Mechanical and Materials Engineering, Washington State University, Pullman, WA 99164, USA

[15] School of Mechanical Engineering, Purdue University, West Lafayette, IN 47907, USA

[16] Department of Macromolecular Science and Engineering, Case Western Reserve University, Cleveland, OH 44106, USA

[17] Department of Chemical and Biomolecular Engineering and Joint Institute for Advanced Materials, University of Tennessee, Knoxville, TN 37996, USA

[18] Center for Nanophase Materials and Sciences, Oak Ridge National Laboratory, Oak Ridge, TN 37830, USA

[19] Department of Mechanical Engineering, University of New Brunswick, Fredericton, New Brunswick E3B 5A3, Canada

[20] Power Generation Laboratory, Korea Electric Power Research Institute, Daejeon 34056, Republic of Korea